

1
2 **Reply to comment on the revised manuscript "The influence of**
3 **particle composition upon the evolution of urban ultrafine diesel**
4 **particles on the neighbourhood scale" by Irina Nikolova et al.**

5
6 We thank the editor and reviewers for their supportive and constructive criticism, which we hope
7 we have addressed fully. We consider each of the editor's final requirements in turn, below. A
8 manuscript tracking the changes we have made in this revision is included in our submission.
9

10 1. There is still a concern that the work is too narrow and perhaps even repetitive to be considered as a stand-
11 alone publication. Authors need to clearly state the unique contributions of the present paper from their previ-
12 ous publication from 2016 mentioned below:

13 <http://pubs.rsc.org/en/content/articlelanding/2016/fd/c5fd00164a/unauth#!divAbstract>. The model framework
14 is the same as in the previous work and so is the application: to assess the influence of a semi-volatile treatment
15 of POA on the evolution of ultrafine aerosol.

16 The 2016 paper cited was very much a preliminary report – we now present a much fuller account, providing not
17 just more results but what we believe is a much more robust conceptual framework. There is no repetition of
18 content between the papers even to the point of leaving the consideration of coagulation and deposition wholly
19 within the 2016 paper. Moreover, the 2016 study was completed before the results of Alam et al. (2016; 2017)
20 from the experimental test rig, which we use here as a strong constraint on the plausibility of particle composi-
21 tions, were available even to us as team members. We draw out the differences between the papers in the fol-
22 lowing lines of the revised manuscript:

23 Introduction: lines 120-122, 125, and 136-138.

24 Methodology: lines 151-152, and 266-267.

25
26 2. To strengthen the reliability of the results, the sensitivity of the threshold modal composition and nucleation
27 mode peak diameter to variations of the mass accommodation coefficient needs to be tested at least for the
28 range between 0.1 and 1 (see the additional review).

29 We have carried out new model runs with varying mass accommodation coefficients (0.01, and
30 0.1), which we report in section 3.4 of the main text, a new figure (Figure 8) and in the SI (Figure 8-
31 S and discussion). We wrap the results of the new model runs into our general discussion: the
32 main conclusion is that we must await further experimental results on vapour pressures or (less
33 likely) accommodation coefficient measurements in order to disambiguate model runs with more
34 volatile vapour pressure parameterisations and lower accommodation coefficients from runs with
35 less volatile vapour pressure parameterisations and higher accommodation coefficients.

36 Please see the following lines of the revised manuscript:

37 Abstract: lines 37 and 50-55.

38 Introduction: lines 136-137

39 Methodology: lines 205-206, and 279-280

40 Results: lines 293 and 445-460 and Figure 8

41 Discussion: lines 468, 501, and 550-554

42 SI: lines 141-149 and Figure 8-S

43

44

45 **Technical corrections in the Supplement:**

46 Line 57 Missing $n(D_p)$ before "is the number of particles per bin width ΔD_p , [# m3]." Done

47 Line 77 Eq. (4) f has to be function of x : $f(x | m, \sigma)$. Done

48 Many thanks to the referee for these corrections.

49

50
51 References for reply
52 Alam, M. S., Rezaei, S. Z., Stark, C. P., Liang, Z., Xu, H. M. and Harrison, R. M.: The characterisation
53 of diesel exhaust particles – composition, size distribution and partitioning, Faraday Discuss., 189,
54 69-84, 2016.
55
56 Alam, M. S., Liang, Z., Rezaei, S. Z., Stark, C. P., Xu, H. M., MacKenzie, A. R. and Harrison, R. M.:
57 Mapping and quantifying isomer sets of hydrocarbons (\geq C12) in diesel fuel, lubricating oil and
58 diesel exhaust samples using GCxGC-ToFMS, Atmos. Meas. Tech. Discuss., submitted, 2017.
59

60

61

62 **The influence of particle composition upon**

63 **the evolution of urban ultrafine diesel**

64 **particles on the neighbourhood scale**

65

66

67 **Irina Nikolova¹, Xiaoming Cai¹, Mohammed Salim Alam¹,**

68 **Soheil Zeraati-Rezaei², Jian Zhong¹, A. Rob MacKenzie^{1,3*}**

69 **and Roy M. Harrison^{1,4}**

70

71

72 **¹School of Geography, Earth and Environmental Sciences**

73 **University of Birmingham, Edgbaston, Birmingham B15 2TT**

74 **United Kingdom**

75

76 **²Department of Mechanical Engineering**

77 **University of Birmingham, Edgbaston, Birmingham B15 2TT**

78 **United Kingdom**

79

80 **³Birmingham Institute of Forest Research (BIFoR)**

81 **University of Birmingham, Edgbaston, Birmingham B15 2TT**

82 **United Kingdom**

83

84 **⁴Also at: Department of Environmental Sciences / Center of Excellence in Environmental**

85 **Studies, King Abdulaziz University, PO Box 80203, Jeddah, 21589, Saudi Arabia**

86

87 *** Corresponding author: a.r.mackenzie@bham.ac.uk**

88

89

90

91 **ABSTRACT**

92 A recent study demonstrated that diesel particles in urban air undergo evaporative shrinkage

93 when advected to a cleaner atmosphere (Harrison et al., Atmospheric Environment, 2016, 125, 1-

94 7). We explore, in a structured and systematic way, the sensitivity of nucleation-mode diesel

95 particles (diameter < 30 nm) to changes in particle composition, saturation vapour pressure, and

96 mass accommodation coefficient. We use a multi-component aerosol microphysics model based

97 on surrogate molecule (C_{16} - C_{32} n-alkane) volatilities. For standard atmospheric conditions (298

98 K, 1013.25hPa), and over timescales (ca. 100 s) relevant for dispersion on the neighbourhood

99 scale (up to 1 km), the choice of a particular vapour pressure dataset changes the range of

100 compounds that are appreciably volatile by 2-6 carbon numbers. The nucleation-mode peak

101 diameter, after 100 s of model runtime, is sensitive to the vapour pressure parameterisations for

102 particles with compositions centred on surrogate molecules between $C_{22}H_{46}$ and $C_{24}H_{50}$. The

103 vapour pressure range, derived from published data, is between 9.23×10^{-3} and 8.94×10^{-6} Pa for

104 $C_{22}H_{46}$ and 2.26×10^{-3} and 2.46×10^{-7} Pa for $C_{24}H_{50}$. The vapour pressures of components in this

105 range are therefore critical for the modelling of nucleation-mode aerosol dynamics on the

106 neighbourhood scale and need to be better constrained. Laboratory studies have shown this

107 carbon number fraction to derive predominantly from engine lubricating oil. The accuracy of

108 vapour pressure data for other (more and less volatile) components from laboratory experiments,

109 is less critical. The influence of a core of non-volatile material is also considered: non-volatile

110 core fractions of more than 5% are inconsistent with the field measurements we test the model

111 against. We consider values of mass accommodation coefficient less than unity and find that

112 model runs with more volatile vapour pressure parameterisations and lower accommodation

113 coefficients are similar to runs with less volatile vapour pressure parameterisations and higher

114 accommodation coefficients. The new findings of this study may also be used to identify the

115 Semi-Volatile Organic Compound (SVOC) compositions that play dominating roles in the

116 evaporative shrinkage of the nucleation mode observed in field measurements (Dall’Osto, et al.,

117 Atmospheric Chemistry & Physics, 2011, 11, 6623-6637).

118 **1. INTRODUCTION**

119 Ultrafine particles (UFP, with particle diameter $D_p < 100 \text{ nm}$) have been increasingly a focus of
120 urban air research over the last two decades. The main source of UFP in outdoor urban air is
121 typically road traffic (Kumar et al., 2014). Harrison et al. (2011) reported that on a busy highway
122 in central London, UK, 71.9% of particles by number were traffic-generated; of which 27.4% are
123 found in the semi-volatile exhaust nucleation mode (size between 15 and 30 nm), 38% are in the
124 exhaust solid mode (size $> 30 \text{ nm}$) and the remaining 6.5% are from brake dust and resuspension
125 (size $> 2000 \text{ nm}$). Hereafter, nucleation mode particles are defined as particles with diameter less
126 than 30 nm, Aitken mode particles have a diameter in the range 30 – 100 nm. The proximity of
127 the UFP traffic source to the public, and the large number of UFP emitted by traffic, have
128 prompted health-related research that has accrued evidence pointing to the toxicity and
129 potentially harmful effects of UFP on human health (Atkinson et al., 2010). Experimental and
130 modelling studies have advanced our understanding of the behaviour of urban air UFP, e.g. the
131 relevant aerosol dynamics important to the evolution of the UFP in space and time (Jacobson,
132 2005; Allen et al., 2007; Biswas et al., 2007; Dall'Osto et al., 2011; Nikolova et al., 2011; Karnezi
133 et al., 2014; Karl et al., 2016).

134

135 Nonetheless, key information regarding the size-resolved composition of the UFP is missing,
136 which limits our ability to determine the impact of gas-transfer processes on UFP evolution.
137 Progress has been made in modelling traffic-generated particles (including the ultrafine fraction)
138 using a volatility basis set, defined using the effective saturation concentration (Donahue et al.,
139 2006). Progress in identifying the precise chemical composition of traffic-generated particles has
140 been made by resolving the so-called ‘unresolved complex mixture’ (largely uncharacterised
141 organics in traditional gas chromatography) via two-dimensional gas chromatography (GC \times GC;
142 Chan et al., 2013). Alam et al. (2016) show that emitted ultrafine diesel particles consist of a
143 substantial amount of organic material from both unburnt diesel fuel and engine lubricating
144 oil. They attribute the low molecular weight Semi-Volatile Organic Compounds (SVOCs, having
145 carbon number < 18) predominantly to the unburnt diesel fuel, whereas heavier SVOCs (carbon

number > 18) are attributed predominantly to the engine lubricating oil. A typical GC \times GC separation is shown in the chromatogram (Figure 1) for diesel engine exhaust emissions in the particulate-phase Aitken mode ($56 < D_p < 100$ nm). Compounds are separated by volatility along the x -axis (first separation dimension) and by polarity in the y -axis (second dimension). Peak identification is based on retention indices and mass spectral data from the National Institute of Standards and Technology (NIST) library. The majority of chromatography peaks (identified as aliphatic alkanes, lower black polygons) are present between C₁₈ to C₂₆, corresponding to the compounds identified in the engine lubricating oil and particulate phase engine emissions (Alam et al. 2017). Bar charts above the chromatogram show the volatility distribution of total alkanes (red) and total identified compounds (black), indicating that, although many hundreds of individual chemical compounds are detected, the majority of the SVOCs emissions consist of alkanes. Both the alkane composition and the total composition distributions show a broad peak centred at C₂₅.

159

160 Most primary organic particle emissions are semi-volatile in nature and thus they are likely to
161 evaporate with atmospheric dilution and moving away from the source (Robinson et al., 2007).
162 This has been observed by Dall'Osto et al. (2011; see also Figure 1-S in Supplementary
163 Information) as part of the REPARTEE campaign (Harrison et al., 2012). Dall'Osto et al. (2011)
164 reported a remarkable decrease in the measured nucleation-mode peak particle diameter ($D_{pg,nuc}$)
165 between a street canyon ($D_{pg,nuc} = 23$ nm) and the downwind neighbourhood ($D_{pg,nuc} = 8\text{--}9$ nm) ca.
166 650 m distant in central London (UK). The travel time, depending on the wind speed, can vary
167 from ~ 100 s to ~ 300 s. Nucleation formation of new particles in the atmosphere was ruled out as
168 a possible reason for the observed behaviour. Instead, the decrease in particle diameter was
169 attributed to the effect of evaporation and substantial mass loss from the particle surface
170 (hereafter referred to as REPARTEE-like aerosol dynamics). Alam et al. (2016) present the
171 composition of diesel UFP particles measured on a laboratory test-rig (cf. Figure 2-S in
172 Supplementary Information), however the range of variability of the particle composition in
173 emissions is still unknown. It is also not known how the organic material is distributed onto the

174 nucleation and Aitken modes of the UFP distribution in the atmosphere.

175

176 Numerical experiments can test the plausibility of possible missing components of the system,
177 and can advise on which experimental studies will be most likely to resolve the existing
178 knowledge gaps. Nikolova et al. (2016) describe a modelling framework that can produce
179 nucleation-mode dynamics consistent with observations. However, missing in that study, which
180 was carried out before the test-rig experimental results (Alam et al., 2016; 2017) were available,
181 is the identificationa systematic sweep of critical thermodynamic parameters and size-resolved
182 composition that could determine or point to a REPARTEE-like aerosol dynamics.

183

184 In the present study, in an extensive new set of model runs moving beyond Nikolova et al.
185 (2016), we develop a method to search the particle composition space — i.e. the volatility
186 parameter space — to identify a group of surrogate n-alkanes in the C₁₆H₃₄-C₃₂H₆₆ range that
187 could explain a decrease in the nucleation-mode particle diameter to 10 nm or below as seen in
188 the measurements in London (Dall'Osto et al., 2011). The model simulations are focused on
189 events after dilution and cooling of the exhaust-pipe plume. We provide a more robust approach
190 to identify crucial parameters responsible for the UFP behaviour in the atmosphere on the
191 neighbourhood scale including the identification of parameter sets that are incompatible with the
192 observed behaviour in urban air of nucleation mode UFP. We describe a new way to simulate and
193 evaluate the role of the SVOCs composition on the atmospheric behaviour of the size-resolved
194 urban UFP and examine more complex sets of composition involving a non-volatile core. We
195 alsoextend our model run set to assess the critical and interacting roles of the saturation vapour
196 pressure parameterisation and the mass accommodation coefficient on the size-resolved aerosol
197 dynamics.

198

199 In this study we use Lagrangian box-model simulations of the evolution of urban ultrafine diesel
200 particles on the neighbourhood scale (up to 1 km). Key results will be presented and discussed
201 here in the main text; more details are provided in the Supplementary Information. The

202 Methodology section describes the modelling approach. The Results section presents the model
203 output. In the Discussion and Conclusions sections, the key findings are summarised with
204 suggestions for further work.

205

206 2. METHODOLOGY

207 We adopt a ‘surrogate molecule’ approach to UFP composition, based on the chemical speciation
208 shown in analyses such as Figure 1. The composition of UFP is simulated as comprising n-
209 alkanes from C₁₆H₃₄ to C₃₂H₆₆, which are the most abundant compounds in Figure 1. Previously
210 (Nikolova et al., 2016), we initialised the n-alkane abundance in gas and particle phases [in a](#)
211 [different way](#), using roadside and urban background observations in Birmingham, U.K. (Harrad
212 et al., 2003). In what follows, we retain this roadside gas-phase initialisation (see below), but
213 choose a more general method for initialising the particle composition, in order to test the
214 sensitivity of the results to the initialisation in a systematic way. By adopting a surrogate
215 molecule approach, we are effectively anchoring [the our](#) model volatility basis set in physico-
216 chemical data, as discussed further below.

217

218 The SVOC mass fractions in a particle are represented by a truncated Gaussian distribution that is
219 centred for each model run at a given n-alkane in the range from C₁₆H₃₄ to C₃₂H₆₆ with a standard
220 deviation, σ , varying from 1 to 5. Below we call the surrogate n-alkane on which the composition
221 distribution is centred, the *modal composition*. Example compositions are shown in Figure 2 for a
222 Gaussian distribution centred at C₂₄H₅₀. A narrower mass distribution, with $\sigma = 1$, focuses
223 predominantly (ca. 40%) on the component, j (C₂₄H₅₀), at which the distribution is centred, with a
224 smaller (ca. 24%) contribution from the adjacent compounds C₂₃H₄₈ and C₂₅H₅₂, and a minor
225 contribution (ca. 5%) from C₂₂H₄₆ and C₂₆H₅₄. The contribution of the remaining compounds
226 from the tail of the distribution is very low and less than 1%. However, a wider mass distribution
227 (e.g. $\sigma = 5$) approximates a flat distribution and includes a contribution from the majority or all of
228 the compounds in the n-alkane range C₁₆H₃₄-C₃₂H₆₆. Monotonically decreasing distributions
229 occur for distributions centred at either end of the C₁₆H₃₄-C₃₂H₆₆ range. Overall, if one excludes

15
16

230 the compounds with less than 1% contribution, modal compositions centred at carbon number, j,
231 with $\sigma = 1, 2, 3, 4, \& 5$, contain surrogate compounds +/- 2, 4, 7, 9, and 11 carbon numbers of j
232 (formally, to remain in the 16-32 carbon number range, [max(16, j-2):min(32, j+2)], [max(16, j-
233 4):min(32, j+4)], [max(16, j-7):min(32, j+7], [max(16, j-9):min(32, j+9], & [max(16, j-
234 11):min(32, j+11)]), respectively. Multi-modal compositions, or others differing strongly from
235 Gaussian, are not investigated in the present study, but could be accommodated by a simple
236 extension of the method.

237

238 We use a Gaussian distribution to represent the composition of the particles because it provides a
239 structured and systematic way to evaluate the organic-aerosol phase partitioning and the amount
240 of organic matter in the UFP. This is important for the behaviour and evolution of the UFP at
241 various timescales relevant for the urban atmosphere. Although there is no reason to discount
242 other functional forms for the composition distribution (e.g., skew Gaussian, log-normal, Pareto,
243 linear, etc), the Gaussian distributions chosen represent a simple two-parameter approach to
244 explore the volatility/composition space available.

245

246 **2.1 Box Model**

247 The model used in this study is the UFP version (Nikolova et al., 2016) of CiTTy-Street (Pugh et
248 al., 2012); that is, a box-model configuration that accounts for the multicomponent nature of the
249 urban ultrafine particles. The CiTTy-Street-UFP model is used with 15 discrete size bins, with an
250 initial diameter range between 5.8-578 nm in a uniform log-scale. The model can operate in two
251 modes with respect to the aerosol dynamics: Eulerian (fixed particle-diameter grid) or Lagrangian
252 (moving particle-diameter grid). The Eulerian mode is selected when the UFP size distribution is
253 evaluated in the presence of emissions and exchange of particles between [spatial](#) boxes (Nikolova
254 et al., 2016). The Lagrangian mode can be selected when the UFP size distribution is evaluated
255 for an isolated air parcel, i.e., when no emissions or transport between [spatial](#) boxes are present.
256 In this study, the Lagrangian mode is selected in a zero-dimensional configuration with no
257 emissions or transport in/out of the box. The UFP dynamics (only condensation/evaporation) are

258 simulated such that particles are allowed to grow/shrink to their exact size without any
259 redistribution onto fixed bins in a grid with bin bounds left open in a fully moving diameter
260 scheme (see, for example, Jacobson et al., 1997). Our earlier work (Nikolova et al., 2016) has
261 shown that deposition and coagulation have a minor effect in the current scenario and so were
262 switched off to allow a more straightforward diagnosis of model behaviour. The
263 condensation/evaporation process applies Raoult's Law (for an ideal solution of the volatile
264 compounds) and a [default](#) mass accommodation coefficient $\alpha = 1$ (Julin et al., 2014) for all
265 SVOC. [The effect of changing \$\alpha\$ is investigated in section 3.4, below.](#) The Kelvin effect is also
266 considered, which alters the saturation vapour pressure of the compounds as a function of the
267 particle diameter, the surface tension of the SVOC mixture/solution, and the molecular weight of
268 the participating compounds. The Kelvin effect is pronounced for particles with a diameter less
269 than 20 nm and substantial for particles with diameter less than 10 nm. The Kelvin term
270 accelerates the evaporation for all compounds under consideration in this study and more notably
271 for the high-molecular-weight compounds due to their larger molar volume.

272 The model results are evaluated at 1, 10 and 100 s. The timescale of 100 s is based on estimate of
273 the travel time on the neighbourhood scale (i.e., horizontal travel distances $\ll 1$ km).

274 **2.2 Modal Composition and Initial Size-Resolved UFP distribution**

275 The initial size-resolved UFP distribution is based on the measurements of Dall'Osto et al. (2011)
276 and reproduced in Figure 1-S in the Supplementary Information. This ultrafine size distribution
277 represents the typical street canyon bimodal size distribution found next to a traffic site, e.g. next
278 to Marylebone Road in London (UK). The distribution has a well-defined nucleation mode with a
279 peak number concentration at $D_{\text{pg,nuc}} \sim 23\text{-}24$ nm. The Aitken mode appears as a shoulder
280 attached to the nucleation mode with a peak number concentration found at $D_{\text{pg,aim}}$ between 50-60
281 nm.

282 The initial UFP size-resolved composition is represented by modal compositions in the range
283 $C_{16}H_{34}\text{-}C_{32}H_{66}$, as detailed above, and a standard deviation σ from 1 to 5. A non-volatile core is
284 included in the ultrafine particles. While studies broadly agree on the existence of a non-volatile
285 core in the Aitken mode (Biswas et al., 2007; Wehner et al., 2004; Ronkko et al., 2013), it is

unclear if nucleation-mode particles contain some non-volatile material or if they are entirely composed of (semi-)volatile SVOC. We have tested the sensitivity to the existence of non-volatile material in the nucleation mode particles by initialising with 1%, 5% or 10% by mass non-volatile material for each modal composition (see Supplementary Information for details of the initialisation); results are discussed later in this paper. Simulations are performed by considering the initialised Aitken mode predominantly non-volatile and coated only with 10% volatile material. This is based on the observations during the REPARTEE campaign (Harrison et al., 2012) that show a fairly stable Aitken mode between the street canyon and the neighbourhood. The initial size-resolved modal compositions, composition standard deviations and non-volatile core in the nucleation and Aitken modes are detailed in Tables 1-S, 2-S, 3-S and 4-S in the Supplementary Information. We also provide information on the input parameters of the log-normal UFP size distribution for Nucleation and Aitken modes.

298

299 **2.3 Saturation Vapour Pressures and Gas-Phase Concentrations**

300 The driving force for condensation/evaporation is the difference between the partial pressure of
301 each representative SVOC and its saturation vapour pressure (hereafter vapour pressure) over the
302 ideal solution in the nucleation mode condensed phase. Figure 3 shows vapour pressures above
303 pure, flat, supercooled liquids for n-alkanes in the range C₁₆H₃₄-C₃₂H₆₆, following Chickos and
304 Lipkind (2008), Compernolle et al. (2011), Lemmon and Goodwin (2000), the Epi Suite
305 calculator (US EPA, 2017), and the UmanSysProp tool (Topping et al., 2016). The UmanSysProp
306 tool provides vapour pressure data based on the work of Nannoolal et al. (2008) and Myrdal and
307 Yalkowsky (1997) with the boiling points of Joback and Reid (1987), Stein and Brown (1994),
308 and Nannoolal et al. (2004). There is a very substantial range of estimated vapour pressures for
309 the same compounds in Figure 3, especially for the high molecular weight n-alkanes. The
310 reported data agrees within an order of magnitude between C₁₆H₃₄ and C₁₉H₄₀, but discrepancies
311 of much more than an order of magnitude are evident for the high molecular weight compounds.
312 The vapour pressure ranges of C₂₂H₄₆ and C₂₄H₅₀ are between [9.23x10⁻³ and 8.94x10⁻⁶ Pa] and
313 [2.26x10⁻³ and 2.46x10⁻⁷ Pa], respectively. An enormous difference in the vapour pressure for

21
22

314 C₃₂H₆₆ (from 2.66x10⁻⁵ Pa in Epi Suite, to 3.20x10⁻¹⁵ Pa in Nannoolal et al., 2008 with the boiling
315 point of Joback and Reid, 1987, called A-a hereafter) is clearly seen in Figure 3. Epi Suite (U.S.
316 Environmental Protection Agency) provides the highest vapour pressures for all selected species
317 in comparison with the rest of the data. Nannoolal et al. (2008) and Myrdal-Yalkowsky (1997)
318 data, both using the boiling point of Joback and Reid (1987), provide similar results and present
319 the lowest vapour pressures among the selected n-alkanes. For the purpose of our sensitivity
320 study, three representative datasets are nominated as input, namely: Myrdal-Yalkowsky (1997)
321 with the boiling point of Nannoolal et al. (2004, called B-c in Figure 3 and hereafter);
322 Compernolle et al. (2011, called Co); and A-a. Hereafter we use the legend abbreviations in
323 Figure 3 when referring to these selected vapour pressures, which are towards the upper, mid-
324 and lower end of the reported data. The vapour pressure from the EPI Suite calculator has been
325 omitted from the analysis below ~~because it has been considered into provide complementarity~~
326 and no duplication of our previous study (Nikolova et al., 2016).

327
328 The gas-phase concentration in the box is initialised with measured gas-phase concentrations in
329 the C₁₆H₃₄-C₃₂H₆₆ range from a traffic site (Harrad et al., 2003) and reported in Table 6-S in the
330 Supplementary Information. For hydroxyl (OH) radical concentration ~10⁶ molec cm⁻³, the
331 timescale for atmospheric oxidation of C₁₆H₃₄ is about 10⁶ s (Atkinson and Arey, 2003).
332 Therefore oxidation of SVOC is neglected given the timescale in our study (100 s). The urban
333 background gas-phase concentration is kept at zero. All model simulations are run at 298 K; the
334 effects of temperature on vapour pressure differences as a function of carbon number are
335 discussed in the Supplementary Information.

336
337 We have performed a total of (17 modal compositions) x (5 σ values) x (3 non-volatile core
338 amounts) x (3 vapour pressures) = 765 + (3 mass accommodation coefficients x 3 vapour
339 pressure parameterisations) = 774 model runs to explore the sensitivity of particle dynamics on
340 the neighbourhood scale.

341

342 The Supplementary Information contains information regarding the initial size distribution,
343 modal composition in the nucleation and Aitken modes, and gas-phase concentrations.
344 Accumulation-mode aerosol (particles diameter $D_p > 100$ nm) is not considered in this study.
345 Accumulation-mode particles have much smaller number concentrations than the nucleation and
346 Aitken modes in polluted urban areas, and are influenced by ageing and transport over larger
347 scales.

348

349 **3. RESULTS**

350 **3.1 Effect of composition on Nucleation-Mode Peak Diameter**

351 We consider first model runs in which the vapour pressure data follows [the mid-range Co](#)
352 [parameterisation](#) (Compernolle et al. (2011), $\alpha = 1$, and nucleation mode particles [are](#) initialised
353 with 1% non-volatile material. The nucleation mode peak diameter $D_{pg,nuc}$ is evaluated at 1 s and
354 100 s of model run-time in runs with varying modal composition and composition standard
355 deviations. Figure 4 shows $D_{pg,nuc}$ (y-axis) at 1s simulation time, for each model run, plotted with
356 respect to the modal composition and composition standard deviation, σ .

357

358 Figure 4 maps out the effect of nucleation-mode composition at this very early stage in the model
359 simulation. For example, at $\sigma = 1$ and initial mass distribution centred at $C_{20}H_{42}$ (green solid line
360 with a square marker), the $D_{pg,nuc}$ decreased from 23 nm (initial diameter at $t = 0$ s) to 12 nm in
361 one second due to evaporation of volatile material from the particles. At $\sigma = 2$, $D_{pg,nuc} = 15$ nm, a
362 somewhat larger diameter than for $\sigma = 1$, due to the inclusion of material of lesser volatility in the
363 particle composition and, hence, a decrease in evaporation overall. For modal compositions
364 between $C_{16}H_{34}$ and $C_{20}H_{44}$, an increase in σ leads to a pronounced deceleration in overall
365 evaporation and, hence, a much larger nucleation mode peak diameter at 1 s simulation time. The
366 opposite effect occurs for modal compositions of $C_{22}H_{46}$ and above, i.e. increasing σ for a given
367 modal composition decreases $D_{pg,nuc}$ at 1 s. This is due to the addition of quickly evaporating
368 lower molecular weight n-alkanes.

369

370 For a modal composition of C₂₁H₄₄, increasing σ makes almost no difference to the model
371 outcome at 1 s. Below, we call the modal composition that shows insensitivity to σ for a given
372 model output time, the *threshold modal composition*. The threshold modal composition points to
373 the composition compound that is in equilibrium between gas and particulate phases for the
374 selected timescale. Lower-carbon-number compositions than the threshold modal composition
375 evaporate quicker and therefore have reached equilibrium with their respective gas concentrations
376 on a much shorter timescale. The higher-carbon-number compositions evaporate slowly and are
377 out-of-equilibrium with their respective gas concentrations for the selected timescale.

378

379 The model output time of 1 s corresponds to the evaporation timescale of C₂₁H₄₄ under the
380 current model setting, in analogy to the e-folding time for an exponentially decaying process.
381 That is, at this time, a significant proportion (e.g. $1-e^{-1} \sim 63\%$ for one e-folding time, and $1-e^{-2} \sim$
382 86% for two e-folding times) of the initial mass has been evaporated. Furthermore, the timescales
383 are much shorter for those lower than C₂₁H₄₄ carbon-number compositions (e.g. C₂₀H₄₂, C₁₉H₄₀,
384 ...) and much longer for those higher than C₂₁H₄₄ carbon-number compositions (e.g. C₂₂H₄₆,
385 C₂₃H₄₈,...).

386

387 To continue the previous example of the modal composition of C₂₀H₄₂, the case with $\sigma = 2$
388 includes not only less volatile materials (i.e. higher-carbon-number SVOCs), but also an equal
389 amount of more volatile materials (i.e. lower-carbon-number SVOCs), as indicated by Figure 2.
390 One might suppose that inclusion of the more volatile material would balance the effect of
391 including less volatile materials. However, following our argument above, most of the lower-
392 carbon-number compounds including C₂₀H₄₂ will have evaporated before the given time of 1 s
393 due to their having much shorter evaporation timescales than C₂₁H₄₄. Thus any material
394 repartitioned from C₂₀H₄₂ to the lower-carbon-number compounds, in changing the model
395 settings from to $\sigma = 1$ to $\sigma = 2$, will not alter the total amount of evaporation and thus the
396 shrinkage rate.

397

398 To take a second example: for C₂₂H₄₆, any material reallocated from C₂₂H₄₆ to the higher-carbon-
399 number compounds (due to changing the model setting from $\sigma = 1$ to $\sigma = 2$) will contribute
400 negligibly to the shrinkage simply because the evaporation timescales for those higher-carbon-
401 number components are much longer than 1 s, whilst the materials repartitioned from C₂₂H₄₆ to
402 the lower-carbon compounds will contribute significantly to evaporation in the first second of
403 model run-time, causing the decreasing trend of the curve shown in Figure 4.

404

405 One implication of this finding is that, if a timescale of 1 s is of interest, the aerosol dynamics of
406 the system is dominated by the threshold modal composition of C₂₁H₄₄. Those lower-carbon-
407 number compositions evaporate in less than 1 s and are approximately in equilibrium with their
408 respective gas concentrations in the environment. The higher-carbon-number compositions
409 evaporate slowly and at this time of 1 s, only a small or a negligible proportion has been
410 evaporated. A few compositions with highest carbon numbers (e.g. C₃₁H₆₄, C₃₂H₆₆) have
411 evaporated almost nothing. Therefore these compositions are effectively non-volatile for these
412 conditions.

413

414 Nucleation-mode particles have an initial non-volatile mass of 2.9 ng m⁻³. Modal compositions
415 from C₁₆H₃₄ to C₁₉H₄₀ and $\sigma = 1$ will lose all their volatile mass in 1 s (Table 1). The initial D_{pg,nuc}
416 decreases from 23 nm to 9 nm and no volatile material is present, i.e. particles are composed of
417 non-volatile core only. Little or no change is simulated in terms of mass and diameter for modal
418 composition C₃₂H₆₆.

419

420 At 100 s, the evaporation of existing mass from the surface of the particles is evident also for
421 higher molecular weight components (Table 1). The D_{pg,nuc} at 100 s is plotted in Figure 5. The
422 diameter has further decreased with a more pronounced drop for all σ and modal compositions up
423 to C₂₅H₅₂. C₂₅H₅₂ is, therefore, the threshold modal composition at this model output time.

424

425 The horizontal line drawn at 10nm on Figure 5 corresponds to evaporation approximating

426 REPARTEE-like behaviour. At $\sigma = 1$, modal compositions in the range C₁₆H₃₄-C₂₃H₄₈ — and
427 vapour pressures and gas-phase partial pressures as detailed in the methodology — could
428 plausibly explain a particle diameter decrease from 23 nm to ~9 nm. Such a narrow range of
429 surrogate molecular compounds is incompatible with experimental observations such as Figure 1.
430 At $\sigma = 2$ and $\sigma = 3$, modal compositions from C₁₆H₃₄ up to C₂₂H₄₆ and C₂₁H₄₄, respectively, can
431 plausibly approximate REPARTEE-like behaviour. At $\sigma = 4$ and $\sigma = 5$ modal compositions from
432 C₁₆H₃₄ up to C₁₉H₄₀ and C₁₇H₃₆, respectively, plausibly simulate REPARTEE-like behaviour.

433

434 **3.2 Effect of Vapour Pressure on the Nucleation-Mode Peak Diameter**

435 We compare the simulated nucleation-mode peak diameter, D_{pg,nuc}, at 100 s using the vapour
436 pressure parameterisations B-c, Co and A-a (cf. Figure 3). The nucleation mode particles are
437 initialised with 1% non-volatile material in these simulations and $\alpha = 1$. Diameter change when
438 using Co vapour pressure has been discussed in the previous section. The values of vapour
439 pressure in the Co data are intermediate between the B-c and A-a data. Hence, D_{pg,nuc} at 100 s
440 using vapour pressure parameterisations A-a and B-c (see Supplementary Information), as
441 expected, shows the same general behaviour as for vapour pressure parameterisation Co, but with
442 a marked change in threshold modal composition. In order of decreasing vapour pressure (Figure
443 3), the 100-s threshold modal composition value changes from C₂₇H₅₆ for the B-c
444 parameterisation (Figure 4-S in the Supplementary Information), to C₂₅H₅₂ for Co (Figure 5), to
445 C₂₂H₄₆ for A-a (Figure 5-S in the Supplementary Information). We restrict ourselves to integer
446 values of threshold modal composition to maintain a straightforward connection back to the
447 homologous chemical series in Figure 1, although there is nothing in principle to prevent us from
448 attributing real number values to the threshold modal composition.

449

450 There is no composition with $\sigma = 4$ and $\sigma = 5$, at the lower volatility A-a vapour pressure
451 parameterisation, that produces REPARTEE-like behaviour; i.e., decrease of the nucleation-mode
452 peak diameter from 23 nm to 10 nm or below. At $\sigma = 5$, the nucleation-mode particles can lose a
453 maximum of ~9 nm of their initial diameter for modal composition C₁₆H₃₄ (please refer to Figure

454 5-S in the Supplementary Information). Little or no change in mode diameter is simulated for
455 modal compositions between C₂₄H₅₀ and C₃₂H₆₆ and $\sigma = 1$, indicating that these combinations of
456 composition and vapour pressure parameterisation are essentially non-volatile for the 100 s
457 simulation time. Modal compositions C₂₀H₄₂ ($\sigma = 1$), C₁₉H₄₀ ($\sigma = 2$) and C₁₇H₃₆ ($\sigma = 3$) can
458 produce REPARTEE-like aerosol dynamics.

459

460 Vapour pressure parameterisation B-c has the highest vapour pressure for all compounds in
461 comparison with Co and A-a. Hence, particles in the nucleation mode are subject to a more
462 pronounced evaporation, even for modal compositions C₂₈H₅₈ to C₃₂H₆₆. Nonetheless, only
463 modal compositions C₂₅H₅₂ ($\sigma = 1$), C₂₄H₅₀ ($\sigma = 2$), C₂₃H₄₈ ($\sigma = 3$), C₂₁H₄₄ ($\sigma = 4$) and C₂₀H₄₂ (σ
464 = 5) are able to produce the REPARTEE-like behaviour. Table 2 provides details on the modal
465 compositions and composition standard deviations that approximate the REPARTEE-like aerosol
466 dynamics for B-c, Co and A-a vapour pressure parameterisations.

467

468 The difference in 100-s D_{pg,nuc} between the highest vapour pressure (B-c) and the lowest vapour
469 pressure (A-a) for all values of σ , is shown in Figure 6. The largest differences (10-14 nm)
470 between the D_{pg,nuc} occur for modal compositions between C₂₂H₄₆ and C₂₄H₅₀ and $\sigma = 1, 2, 3$. For
471 model run-time of 100 s, the variability of the UFP shrinkage due to the uncertainty of vapour
472 pressure data is highest for the compositions between C₂₂H₄₆ and C₂₄H₅₀. From Figure 3, we see
473 that the uncertainty of vapour pressure data increases monotonically with carbon number and is
474 highest for C₃₂H₆₆. However, this high level of large vapour-pressure uncertainty for high-
475 carbon compositions does not exert a significant impact on the model results for this scenario. We
476 thus conclude that the accuracy of vapour pressure values for very high or very low carbon-
477 number compositions are not important for neighbourhood-scale aerosol dynamics.

478

479 **3.3 Effect of Non-Volatile Core on the Nucleation Mode Peak Particle Diameter**

480 To consider how the fraction of non-volatile core interacts with the SVOCs composition and the
481 vapour pressure parameterisations, we define a ‘100-s effective non-volatile core’: the nucleation

482 mode peak diameter at 100 s of evaporation. Figure 7 shows results for three non-volatile
483 fractions (initial 1%, 5% and 10% based on mass) and vapour pressures A-a, B-c and Co (cf.
484 Figure 3), for a modal composition of C₁₆H₃₄. Results for the remaining modal compositions are
485 not plotted here because using modal composition C₁₆H₃₄ and an evaporation time of 100 s gives
486 the maximum reduction of the nucleation-mode peak diameter for all σ in our model runs.
487 However, we show the results for modal compositions C₂₄H₅₀ and C₃₂H₆₆ for completeness in the
488 Supplementary Information (Figure 7-S).

489
490 Because the mass-size distribution is held constant for each model initialisation (see
491 Supplementary Information), an increase of the non-volatile material in the nucleation mode
492 leads to a decrease in the total amount of n-alkane SVOC available for evaporation, and hence
493 leads to an increase in the nucleation mode ‘dry’ (i.e. non-volatile core only) diameter from ~9
494 nm to ~12 nm. For the lowest volatility parameterisation (A-a), only the lightest surrogate
495 compounds near C₁₆H₃₄ are sufficiently volatile over the timescale of the model run to drive
496 evaporation of nucleation mode particles. As σ increases, an increasing number of lower
497 volatility components are added into the particle composition, causing the 100-s effective non-
498 volatile core to increase.

499
500 Considering REPARTEE-like behaviour, i.e., shrinkage of the nucleation mode diameter to ca.
501 10 nm, initial non-volatile core fractions of 5% or greater do not reproduce the observed
502 behaviour.

503
504 **3.4 Effect of mass accommodation coefficient less than unity**

505 The effect of reducing the value of the mass accommodation coefficient from the default value of
506 unity, is shown in Figure 8 as a function of modal standard deviation and vapour pressure, for a
507 modal composition of C₁₆H₃₄. Considering first our default Co vapour pressure parameterisation,
508 using $\alpha = 1$ results in rapid evaporation and small D_{pg,nuc} for 1 < σ < 5. As discussed in section
509 3.1, above, such combinations of modal composition and vapour pressure parameterisation

510 produce a very volatile nucleation-mode aerosol that evaporates 'to dryness' over the course of the
511 model run. Decreasing the value of the mass accommodation coefficient decreases the effective
512 volatility of the model runs with Co vapour pressure (Figure 8), leading to larger values of $D_{pg,nuc}$.
513 Similarly, end-of-run values of $D_{pg,nuc}$ increase with decreasing values of α for the A-a and B-c
514 vapour pressure parameterisations. The overall effect is such that model runs using the higher
515 volatility B-c parameterisation and $\alpha = 0.1$ match results using the Co vapour pressures and $\alpha = 1$.
516 Similarly, model runs using the lower volatility A-a parameterisation and $\alpha = 1$ match results
517 using the Co vapour pressures and $\alpha = 0.01$. Determining which combination of vapour pressure
518 and mass accommodation is more realistic requires further laboratory experiments to constrain
519 these properties.

520

521 4. DISCUSSION AND CONCLUSIONS

522 The purpose of this study was to evaluate the importance of particle composition and saturation
523 vapour pressure on the evolution of urban ultrafine diesel particles on the neighbourhood scale
524 ($<< 1 \text{ km}$) by means of numerical simulations. We present the effect of evaporation on the size-
525 resolved ultrafine particles and looked at the evolution of the nucleation-mode peak diameter
526 $D_{pg,nuc}$ depending on particle SVOC composition, vapour pressure, and fraction of non-volatile
527 core in the particles, and the value of the mass accommodation coefficient. We have used
528 laboratory measurements of the size-resolved composition of the ultrafine particles as an
529 additional strong constraint on the plausibility of model parameter sets. We identified a group of
530 surrogate n-alkane compounds in the range $C_{16}H_{34}$ - $C_{32}H_{66}$ that could explain REPARTEE-like
531 aerosol dynamics measured in London (Dall'Osto et al., 2011): i.e., a final nucleation-mode peak
532 diameter at 10 nm or below when particles were subject to evaporation in a timescale of 100 s.
533 Table 2 highlighted the set of parameters in terms of vapour pressure and modal compositions
534 that produce such REPARTEE-like behaviour.

535

536 Table 2 presents the sets of model parameters consistent with diameter reduction due to
537 evaporation. The question remains, however, to what extent these results are realistic and relevant

for the real-world atmosphere. Standard deviation $\sigma = 1$ for all vapour pressures narrows significantly the contribution from the n-alkanes ([max(16, j-2):min(32, j+2)] for modal composition j), present in the initial composition of the nucleation mode particles. At $\sigma = 2$, the main contributing compounds involved in particle composition are the modal composition j and the surrogate molecules [max(16, j-4):min(32, j+4)]. This means that for the given vapour pressure parameterisation, A-a, and modal composition C₁₉H₄₀, the compounds found in the particles would be between C₁₅H₃₂ and C₂₃H₄₈. However, C₁₆H₃₄ is the lower limit of surrogate compounds in the model, so the Gaussian distribution of composition is truncated at the low-carbon-number end in this case. At $\sigma = 3$, the contributing compounds found in the particles are the surrogate molecules in the range [max(16, j-7):min(32, j+7)]. For a modal composition C₁₇H₃₆ and A-a vapour pressure, the range of participating compounds is C₁₆H₃₄-C₂₄H₅₀, similar to the case of $\sigma = 2$. At $\sigma = 4$ and 5, the majority of the surrogate molecules in our range of n-alkanes participate in the composition of particles, thus providing a reasonable range over the contribution from diesel fuel and engine lubricating oil. The range at $\sigma = 3$ could be considered as a transition range, while examples at $\sigma = 2$ would have compositions that are rather more limited than available measurements in the Aitken mode (e.g. Figure 1), with a focus on the contribution from the engine lubricating oil. Overall, narrow compositions would imply a strong gradient of SVOCs across the nucleation and Aitken modes whereas broad compositions imply that SVOCs are more or less evenly distributed across the ultrafine size range.

Table 3 shows an additionally constrained range of modal compositions consistent with what we know from field and laboratory measurements combined. The lowest vapour pressure parameterisations (A-a and the very similar B-a, see Figure 3) are less likely, at any modal composition standard deviation (σ) [and mass accommodation coefficient](#), to represent the laboratory and field observations together. The results reported in Alam et al. (2016) and in Figure 1 show that diesel ultrafine particle emissions are composed of a wealth of SVOCs that are mainly identified as straight and branched alkanes in the range C₁₁-C₃₃, cycloalkanes (C₁₁-C₂₅), PAHs, various cyclic aromatics, alkyl benzenes and decalins. They report emitted particulate size fractionated concentrations of n-alkanes (cf. Figure 2-S in Supplementary Information) and point

566 out that particles in the 5–100 nm diameter range consist mainly of high molecular weight SVOCs
567 ($>\text{C}_{24}\text{H}_{50}$) associated with engine lubricating oil. The work of Robinson et al. (2007), Grishop et
568 al. (2009) and May et al. (2013) also point to a Gaussian-type distribution of the exhaust particle
569 composition centred at SVOC, that has a wide standard deviation.

570

571

572 Vapour pressure parameterisations used in this study and plotted in Figure 3, are one of the
573 crucial input parameters in assessing the rate at which condensation/evaporation can occur,
574 though they are poorly constrained. We introduced a new concept of threshold modal
575 composition, i.e. modal composition that is not sensitive to σ for a given model output time. In an
576 order of decreasing vapour pressure (Figure 3) and timescale of 100 s, the threshold modal
577 composition value changes from $\text{C}_{27}\text{H}_{56}$ for the B-c parameterisation (Figure 4-S, Supplementary
578 Information), to $\text{C}_{25}\text{H}_{52}$ for Co (Figure 5), to $\text{C}_{22}\text{H}_{46}$ for A-a (Figure 5-S, Supplementary
579 Information). Overall, the largest differences (~ 14 nm) in the 100-s $D_{\text{pg,nuc}}$ occur between the
580 highest (B-c) and the lowest (A-a) vapour pressure parameterisations for modal compositions
581 between $\text{C}_{22}\text{H}_{46}$ and $\text{C}_{24}\text{H}_{50}$ and composition standard deviation from 1 to 3. The vapour
582 pressures of components in this range are therefore critical for the modelling of nucleation-mode
583 aerosol dynamics on the neighbourhood scale. For components with volatility less than that for
584 the $\text{C}_{22}\text{H}_{46}$ surrogate compound used here, all available vapour pressure parameterisations render
585 these compounds volatile over the 100-s timescale. These components will equilibrate with the
586 gas phase on these short timescales. Components with volatility lower than that of the $\text{C}_{24}\text{H}_{50}$
587 surrogate are effectively non-volatile over this timescale for all vapour pressure
588 parameterisations, and so will remain condensed and out-of-equilibrium with the gas phase on
589 these timescales.

590

591 The other variable which will influence evaporation rate is the concentration of vapour
592 surrounding the particles. In this work, measured roadside vapour concentrations reported by
593 Harrad et al. (2003) are used (see also Nikolova et al., 2016). These represent an upper estimate

594 of gas-phase partial pressures away from roadside. Mixing of cleaner urban background air into
595 the simulated air parcel would lower partial pressures and increase evaporation rates.

596

597 The 100-s effective non-volatile core (the nucleation mode peak diameter at 100 s of evaporation)
598 increased from ~9 nm to ~12 nm. This was attributed to the decrease in the total amount of n-
599 alkane surrogate compounds present for evaporation. As composition standard deviation σ
600 increased, an increasing number of lower volatility components added into the particle
601 composition caused the 100-s effective non-volatile core to further increase. Considering
602 REPARTEE-like behaviour, i.e., shrinkage of the nucleation mode diameter to ca. 10 nm, an
603 initial non-volatile core of 5% by mass or greater was not capable of reproducing the observed
604 behaviour in the atmosphere. Because the higher molecular weight (lower volatility) surrogate
605 molecules in the model are essentially non-volatile over the modelling timescale, the nucleation
606 mode dynamics due to SVOC is confounded with that due to the size of any non-volatile core
607 present in the particles.

608

609 We find that, the model results for a given vapour-pressure parameterisation vary markedly
610 depending on the choice of value for the mass accommodation coefficient, α . Higher volatility
611 vapour-pressure parameterisations with low values of α give model results similar to runs with
612 less volatile vapour-pressure parameterisations and higher values of α . Such equifinality in model
613 runs awaits further laboratory work to disambiguate.

614

615 Results (Figure 7) suggest that urban nucleation mode particles should be predominantly volatile
616 in order to produce REPARTEE-like behaviour. In these numerical experiments, the nature of the
617 non-volatile core need not be specified. This core could be composed of one or more low vapour
618 pressure compounds, not affected by condensation/evaporation on the timescale of the model and
619 measurements. On the other hand, as discussed in Nikolova et al. (2016), a non-volatile core
620 could be composed mainly of carbon and possibly some contribution from metal oxides and
621 sulphates. This difference in composition could be relevant to effects on human health. Li et al.

622 (2010) show that diesel truck emissions during idle induce a high level of oxidative stress in
623 human aortic endothelial cells, due to the type of metals and trace metals found in the exhaust,
624 while Xia et al. (2015) argue that traffic-related UFP act to promote airway inflammation due to
625 the rich content of organic species. The relative importance of these particles in affecting human
626 health merits further investigations.

627

628 Laboratory exhaust diesel ultrafine particulate measurements are highly dependent on the
629 sampling methods. Measurements of the ultrafine particle composition from a diesel-fuelled
630 engine are still at an early stage and therefore more efforts should be put into developing
631 sampling protocols that target the composition of the nucleation and Aitken modes particles in a
632 realistic manner. There are no robust UFP chemical composition measurements at street scale and
633 therefore such measurements devoted to address in detail the composition of the traffic emitted
634 UFP in the atmosphere are urgently needed. Saturation vapour pressure is another source of large
635 uncertainties; our study lays out a strategy to determine which vapour pressures are most
636 significant in a given modelling scenario.

637

638

639 **ACKNOWLEDGEMENTS**

640 This work is part of the FASTER project, ERC-2012-AdG, Proposal No. 320821 sponsored by
641 the European Research Council (ERC).

642

643

644

645

646

647

648

649

- 650
651
652
- 653 **REFERENCES**
- 654
- 655 Alam, M. S., Rezaei, S. Z., Stark, C. P., Liang, Z., Xu, H. M. and Harrison, R. M.: The
656 characterisation of diesel exhaust particles – composition, size distribution and partitioning,
657 Faraday Discuss., 189, 69-84, 2016.
- 658
- 659 Alam, M. S., Liang, Z., Rezaei, S. Z., Stark, C. P., Xu, H. M., MacKenzie, A. R. and Harrison, R.
660 M.: Mapping and quantifying isomer sets of hydrocarbons (\geq C12) in diesel fuel, lubricating oil
661 and diesel exhaust samples using GC \times GC-ToFMS, Atmos. Meas. Tech. Discuss., submitted,
662 2017.
- 663
- 664 Allen, L. R., Donahue, N. M., Shrivastava, M. K., Weitkamp, E. A., Sage, A. M., Grieshop, A.
665 P., Lane, T. E., Pierce, J. R. and Pandis, S. N.: Rethinking organic aerosols: semivolatile
666 emissions and photochemical aging. Science, 315, 1259-62, 2007.
- 667
- 668 Atkinson, R. W., Fuller, G. W., Anderson, H. R., Harrison, R. M. and Armstrong, B.: Urban
669 ambient particle metrics and health: a time-series analysis, Epidemiology, 21, 501-511, 2010.
- 670
- 671 Biswas, S., Ntziachristos, L., Moore, K. F. and Sioutas, C: Particle volatility in the vicinity of a
672 freeway with heavy-duty diesel traffic, Atmos. Environ., 41, 3479-3493, 2007.
- 673
- 674 Chan, A. W. H., Isaacman, G., Wilson, K. R., Worton, D. R., Ruehl, C. R., Nah, T., Gentner, D.
675 R., Dallmann, T. R., Kirchstetter, T. W., Harley, R. A., Gilman, J. B., Kuster, W. C., de Gouw, J.
676 A., Offenberg, J. H., Kleindienst, T. E., Lin, Y. H., Rubitschun, C. L., Surratt, J. D., Hayes, P. L.,
677 Jimenez, J. L. and Goldstein, A. H.: Detailed chemical characterization of unresolved complex

- 678 mixtures in atmospheric organics:insights into emission sources, atmospheric processing, and
679 secondary organic aerosol formation, J. Geophys. Res.:Atmospheres, 118, 6783-6796, 2013.
- 680
- 681 Chickos, J. and Lipkind, D.: Hypothetical thermodynamic properties: vapour pressures and
682 vaporization enthalpies of the even n-Alkanes from C78 to C92 at T= 298.15K by correlation-gas
683 chromatography, J. Chem. Eng. Data, 53, 2432-2440, 2008.
- 684
- 685 Compernolle, S., Ceulemans, K. and Muller, J. -F.: Evaporation: a new vapour pressure
686 estimation method for organic molecules including non-additivity and intramolecular
687 interactions, Atmos. Chem. Phys., 11, 9431-9450, 2011.
- 688
- 689 Dall'Osto, M., Thorpe, A., Beddows, D.C.S., Harrison, R.M., Barlow, J.F., Dunbar, T., Williams,
690 P.I. and Coe, H.: Remarkable dynamics of nanoparticles in the urban atmosphere, Atmos. Chem.
691 Phys., 11, 6623-6637, 2011.
- 692
- 693 Donahue, N. M., Robinson, A. L., Stanier, C. O., and Pandis, S. N.: Coupled partitioning,
694 dilution, and chemical aging of semivolatile organics, Environ. Sci. Technol., 40, 2635–2643,
695 2006.
- 696
- 697 Grieshop, A., Miracolo, M., Donahue, N., and Robinson, A.: Constraining the volatility
698 distribution and gas-particle partitioning of combustion aerosols using isothermal dilution and
699 thermodenuder measurements., Environ. Sci. Technol., 43, 4750, 2009.
- 700
- 701 Harrad, S., Hassoun, S., Callen Romero, M.S. and Harrison, R.M.: Characterisation and source
702 attribution of the semi-volatile organic content of atmospheric particles and associate
703 vapour phase in Birmingham, UK, Atmos. Environ., 37, 4985-4991, 2003.
- 704
- 705 Harrison, R. M., Beddows, D. S. and Dall'Osto, M.: PMF analysis of wide-range particle size

- 706 spectra collected on a major highway, Environ. Sci. Technol., 45, 5522-5528, 2011.
- 707
- 708 Harrison, R. M., Dall'Osto, M., Beddows, D. C. S., Thorpe, A. J., Bloss, W. J., Allan, J. D., Coe,
709 H., Dorsey, J. R., Gallagher, M., Martin, C., Whitehead, J., Williams, P. I., Jones, R. L.,
710 Langridge, J. M., Benton, A. K., Ball, S. M., Langford, B., Hewitt, C. N., Davison, B., Martin,
711 D., Petersson, K. F., Henshaw, S. J., White, I. R., Shallcross, D. E., Barlow, J. F., Dunbar, T.,
712 Davies, F., Nemitz, E., Phillips, G. J., Helfter, C., Di Marco C. F. and Smith, S.: Atmospheric
713 chemistry and physics in the atmosphere of a developed megacity (London): an overview of the
714 REPARTEE experiment and its conclusions, Atmos. Chem. Phys., 12, 3065-3114, 2012.
- 715
- 716 Harrison, R.M., Jones, A.M., Beddows, D.C.S., Dall’Osto M. and Nikolova, I.: Evaporation of
717 traffic-generated nanoparticles during advection from source, Atmos. Environ., 125, 1-7, 2016.
- 718
- 719 Joback, K. and Reid, R.: Estimation of Pure-component properties from group-contributions,
720 Chem. Eng. Commun., 57, 233-243, 1987.
- 721
- 722 Jacobson, M.Z.: Development and application of a new air pollution modeling system. 2. Aerosol
723 module structure and design, Atmos. Environ., 31, 131-144, 1997.
- 724
- 725 Jacobson, M. Z., Kittelson, D. B., and Watts, W. F.: Enhanced coagulation due to evaporation
726 and its effect on nanoparticle evolution, Environ. Sci. Technol., 39, 9486- 9492, 2005.
- 727
- 728 Julin, J., Winkler, P. M., Donahue, N. M., Wagner, P. E. and Riipinen, I.: Nera-unity mass
729 accomodation coefficient of organic molecules of varying structure, Environ. Sci. Technol., 48,
730 12083-12089, 2014.
- 731
- 732 Karl, M., Kukkonen, J., Keuken, M. P., Lützenkirchen, S., Pirjola, L., and Hussein, T.: Modeling
733 and measurements of urban aerosol processes on the neighborhood scale in Rotterdam, Oslo and

- 734 Helsinki, Atmos. Chem. Phys., 16, 4817-4835, doi:10.5194/acp16-4817-2016, 2016.
- 735
- 736 Karnezi, E., Riipinen, I. and Pandis, S. N.: Measuring the atmospheric organic aerosol volatility
737 distribution: a theoretical analysis, Atmos. Meas. Tech. Discuss., 7, 2953-2965, 2014.
- 738
- 739 Kumar, P., Morawska, L., Birmili, W., Paasonen, P., Hu, M., Kulmala, M., Harrison, R. M.,
740 Norford, L. and Britter, R.: Ultrafine particles in cities, Environ. Intl., 66, 1-10, 2014.
- 741
- 742 Lemmon, E. W. and Goodwin, A. R. H.: Critical properties and vapour pressure equation for
743 alkanes C_nH_{2n+2}: normal alkanes with n ≤ 36 and isomers for n = 4 through n = 9, J. Phys.
744 Chem. Ref. Data, 29, 1-39, 2000.
- 745
- 746 Li, R., Ning, Z., Majumdar, R., Cui, J., Takabe, W., Jen, N., Sioutas, C. and Hsiai, T.: Ultrafine
747 particles from diesel vehicle emissions at different driving cycles induce differential vascular pro-
748 inflammatory responses: implications of chemical components and NF-κB signaling, Part. Fibre
749 Toxicol., 7-6, 2010.
- 750
- 751 May, A. A., Presto, A. A., Hennigan, C. J., Nguyen, N. T., Gordon, T. D., and Robinson, A. L.:
752 Gas-particle partitioning of primary organic aerosol emissions: (2) Diesel vehicles, Environ. Sci.
753 Technol., 47, 8288-8296, 2013.
- 754
- 755 Myrdal, P. B. and Yalkowsky, S. H.: Estimating pure component vapor pressures of complex
756 organic molecules, Ind. Eng. Chem. Res., 36, 2494-2499, 1997.
- 757
- 758 Nannoolal, Y., Rarey, J., Ramjugernath, D. and Cordes, W.: Estimation of pure component
759 properties: Part 1. Estimation of the normal boiling point of non-electrolyte organic compounds
760 via
761 group contributions and group interactions, Fluid Phase Equilibr., 226, 45-63, 2004.

- 762
763 Nannoolal, Y., Rarey, J. and Ramjugernath, D.: Estimation of pure component properties: Part 3.
764 Estimation of the vapor pressure of non-electrolyte organic compounds via group contributions
765 and group interactions, *Fluid Phase Equilibr.*, 269, 117-133, 2008.
766
767 Nikolova, I., Janssen S., Vos, P., Vrancken, K., Mishra, V. and Berghmans, P.: Dispersion
768 modelling of traffic induced ultrafine particles in a street canyon in Antwerp, Belgium and
769 comparison with observations, *Sci. Total Environ.*, 412-413, 336-43, 2011.
770
771 Nikolova, I., MacKenzie, A. R., Cai, X., Alam, M. S. and Harrison, R. M.: Modelling component
772 evaporation and coposition change of traffic-induced ultrafine particles during travel from street
773 canyon to urban background, *Faraday Discuss.*, 189, 529-546, 2016.
774
775 Pugh, T. A. M., MacKenzie, A. R., Whyatt, J. D. and Hewitt, C. N.: Effectiveness of green
776 infrastructure for improvement of air quality in urban street canyons, *Environ. Sci. Technol.*, 46,
777 7692-7699, 2012.
778
779 Robinson, A. L., Donahue, N. M., Shrivastava, M. K., Weitkamp, E. A., Sage, A. M., Grieshop,
780 A. P., Lane, T. E., Pierce, J. R. and Pandis, S. N.: Rethinking organic aerosols: semivolatile
781 emissions and photochemical aging, *Science*, 315, 1259-1262, 2007.
782
783 Ronkko, T., Lahde, T., Heikkila, J., Pirjola, L., Bauschke, U., Arnold, F., Schager, H., Rothe, D.,
784 Yli-Ojanpera, J. and Keskinen, J.: Effects of Gaseous Sulphuric Acid on Diesel Exhaust
785 Nanoparticle Formation and Characteristics, *Environ. Sci. Technol.*, 47, 11882-11889, 2013.
786
787 Stein, S. E. and Brown, R. L.: Estimation of normal boiling points from group contributions, *J.*
788 *Chem. Inf. Comp. Sci.*, 34, 581-58, 1994.
789

790 Topping, D., Barley, M., Bane, M. K., Higham, N., Aumont, B., Dingle, N., and McFiggans, G.:
791 UManSysProp v1.0: an online and open-source facility for molecular property prediction and
792 atmospheric aerosol calculations, *Geosci. Model Dev.*, 9, 899-914, 2016.
793
794 US EPA: Estimation Programs Interface Suite™ for Microsoft® Windows, v 4.11, United States
795 Environmental Protection Agency, Washington, DC, USA, 2017.
796
797 Wehner, B., Philippin, S., Wiedensohler, A., Scheer, V. and Vogt, R.: Variability of non-volatile
798 fractions of atmospheric aerosol particles with traffic influence, *Atmos. Environ.*, 38, 6081-6090,
799 2004.
800
801 Xia, M., Viera-Hutchins, L., Garcia-Lloret, M., Rivas, M. N., Wise, P., McGhee, S. A., Chatila,
802 Z. K., Daher, N., Sioutas, C. and Chatila, T. A.: Vehicular exhaust particles promote allergic
803 airway inflammation through an aryl hydrocarbon receptor-notch signaling cascade, *J. Allergy*
804 *Clin. Immun.*, 136, 441-453, 2015.
805
806 **TABLE LEGENDS**
807 **Table 1.** Total mass M (ng m^{-3}) of nucleation mode peak particles at 1 s and 100 s of
808 simulation for modal compositions $C_{16}\text{H}_{34}$ - $C_{32}\text{H}_{66}$ and composition standard
809 deviations, sigma. For comparison, the initial mass of the non-volatile material in the
810 nucleation mode peak particles is 2.9 ng m^{-3} .
811
812 **Table 2.** Modal composition ranges and composition standard deviations, sigma, producing
813 model results that approximate REPARTEE-like behaviour (see main text), for
814 different vapour pressure parameterisations. Initial non-volatile core in the nucleation
815 mode is set to 1%.
816

817 **Table 3.** Modal composition range and composition standard deviations, sigma, producing
818 more realistic results that approximate REPARTEE-like behaviour. Vapour pressure
819 parameterisation follows Myrdal and Yalkowski (1997; B-c in Figure 3),
820 Compernolle et al. (2011; Co in Figure 3), and Nannoolal 2008; A-a in Figure 3).
821 Column 'cn' indicates the carbon number of compounds n in the modal composition
822 with a contribution bigger than 1%.

823

824

825 **FIGURE LEGENDS**

826 **Figure 1.** A GC×GC chromatogram (contour plot) indicating homologous series of compounds
827 identified in diesel engine exhaust emissions. Emissions from a light-duty diesel
828 engine operating at 1800 revolutions per minute and 1.4 bar brake mean effective
829 pressure. Compounds identified in the contour plot are indicated by the coloured
830 polygons – Lower black polygons are n- + i-alkanes; red polygons are monocyclic
831 alkanes; green polygons are bicyclic alkanes; pink polygons are aldehydes + ketones;
832 and upper black polygons are monocyclic aromatics. Each peak in the contour plot
833 represents a compound present in the emissions; warmer colours (e.g. red) are more
834 intense peaks while colder colours (blue) are smaller peaks. Contour plot were
835 produced by GC Image v2.5. Bar charts above show the volatility distribution of total
836 alkanes (red) and total identified species (black), indicating that the majority of the
837 emissions consist of alkanes. For details of the compound attribution method, see
838 Alam et al. (2017).

839

840 **Figure 2.** An example of nucleation mode UFP compositions, represented as mass fractions for
841 surrogate compounds $C_nH_{(2n+2)}$, $n = [16:32]$, and described by a Gaussian distribution
842 centred on $C_{24}H_{50}$ with standard deviation, σ , from 1 to 5.

843

844 **Figure 3.** Vapour pressure data for selected n-alkanes $C_nH_{(2n+2)}$ where $n = [16:32]$ at 298K.

845 Abbreviations in the legend point to the source as follows: A and B refer to
846 the vapour pressure data from Nannoolal et al. (2008) and Myrdal and
847 Yalkowsky (1997), respectively; -a, -b and -c refer to the boiling point of Joback
848 and Reid (1987), Stein and Brown (1994) and Nannoolal et al. (2004),
849 respectively; ES refers to Epi Suite calculator (U.S. Environmental Protection
850 Agency); Co to Compernolle et al. (2011); Ch to Chickos and Lipkind (2008), LG to
851 Lemmon and Goodwin (2000).

852

853 **Figure 4.** Nucleation mode peak diameter D_p [nm] at 1 s of simulation depending on the modal
854 composition and the composition standard deviation. The initial nucleation mode
855 peak diameter is at 23nm (not shown on the figure).Vapour pressure data follows
856 Compernolle et al. (2011).

857

858 **Figure 5.** Nucleation mode peak diameter D_p [nm] at 100 s of simulation depending on the
859 modal composition and the composition standard deviation. The initial nucleation
860 mode peak diameter is at 23nm (not shown on the figure).Vapour pressure data
861 follows Compernolle et al. (2011).

862

863 **Figure 6.** $D_{pg,nuc}$ difference between the nucleation mode peak diameter (nm) when using B-c
864 vapour pressure and the nucleation mode peak diameter when using A-a vapour
865 pressure for modal compositions $C_nH_{(2n+2)}$ where $n = [16:32]$.

866

867 **Figure 7.** Nucleation mode peak diameter D_p [nm] at 100 s: the ‘100-s effective non-volatile
868 core’ for the nucleation mode. Results are shown at 1%, 5% and 10% initial non-
869 volatile material in the nucleation mode particles, modal composition $C_{16}H_{34}$ and for
870 various composition standard deviations.

871 [Figure 8.](#) Nucleation mode peak diameter D_p [nm] at 100 s of simulation depending on the mass
872 accommodation coefficient, the vapour pressure parameterisation, and the composition standard
873 deviation. The initial nucleation mode peak diameter is at 23 nm (not shown on the figure).
874 Results are shown for 1% initial non-volatile material in the nucleation mode particles, modal
875 composition C₁₆H₃₄, and for various composition standard deviations. The vapour pressure
876 parameterisations are labelled as for Figure 3.

877

878

879	1s		C ₁₆ H ₃₄	C ₁₇ H ₃₆	C ₁₈ H ₃₈	C ₁₉ H ₄₀	C ₂₀ H ₄₂	C ₂₁ H ₄₄	C ₂₂ H ₄₆	C ₂₃ H ₄₈	C ₂₄ H ₅₀	C ₂₅ H ₅₂	C ₂₆ H ₅₄	C ₂₇ H ₅₆	C ₂₈ H ₅₈	C ₂₉ H ₆₀	C ₃₀ H ₆₂	C ₃₁ H ₆₄	C ₃₂ H ₆₆	
880	Centre @	Sigma	1	2.9	2.9	2.9	2.9	7.4	23.6	38.1	46.8	51.0	52.6	53.2	53.4	53.5	53.5	53.5		
881			2	2.9	2.9	3.2	6.9	14.3	24.1	34.0	42.1	47.0	50.3	52.1	52.9	53.3	53.4	53.5	53.5	
882			3	3.7	5.4	8.4	12.9	18.5	24.9	31.6	38.1	43.5	46.8	49.3	51.0	52.1	52.8	53.1	53.3	53.4
			4	8.0	10.6	13.7	17.6	21.8	26.4	31.0	35.4	39.7	43.7	46.2	48.2	49.8	50.9	51.8	52.3	52.7
			5	12.8	15.3	18.1	21.1	24.4	27.7	31.2	34.4	37.6	40.2	43.0	45.4	47.0	48.4	49.5	50.4	51.2
883	100s																			
884	Centre @	Sigma	1	2.9	2.9	2.9	2.9	2.9	2.9	2.9	2.9	6.1	23.8	38.9	47.5	51.3	52.8	53.3	53.5	53.6
885			2	2.9	2.9	2.9	2.9	2.9	2.9	3.0	6.2	14.3	24.8	34.8	42.5	47.6	50.6	52.1	52.9	53.2
886			3	2.9	2.9	2.9	2.9	3.1	4.2	7.1	11.9	18.2	25.2	31.9	37.8	42.6	46.1	48.6	50.3	51.4
			4	2.9	3.0	3.3	4.1	5.6	7.9	11.1	15.1	19.7	24.6	29.3	33.8	37.7	41.1	43.8	46.1	47.8
			5	3.7	4.4	5.4	6.9	8.7	11.1	13.8	17.0	20.2	23.7	27.2	30.6	33.7	36.6	39.2	41.4	43.4

887

888 **Table 1.** Total mass M (ng m⁻³) of nucleation mode peak particles at 1 s and 100 s of simulation
889 for modal compositions C₁₆H₃₄-C₃₂H₆₆ and composition standard deviations, sigma. For
890 comparison, the initial mass of the non-volatile material in the nucleation mode peak particles is
891 2.9 ng m⁻³.

892

893

894

895

896

	Vapour pressure Sigma	B-c	Co	A-a
897	1	$\leq C_{28}H_{52}$	$\leq C_{23}H_{48}$	$\leq C_{20}H_{42}$
898	2	$\leq C_{24}H_{50}$	$\leq C_{22}H_{46}$	$\leq C_{19}H_{40}$
899	3	$\leq C_{23}H_{48}$	$\leq C_{21}H_{44}$	$\leq C_{17}H_{36}$
900	4	$\leq C_{21}H_{44}$	$\leq C_{19}H_{40}$	-
	5	$\leq C_{20}H_{42}$	$\leq C_{17}H_{36}$	-

901

902 **Table 2.** Modal composition ranges and composition standard deviations, sigma, producing
 903 model results that approximate REPARTEE-like behaviour (see main text), for different vapour
 904 pressure parameterisations. Initial non-volatile core in the nucleation mode is set to 1%.

905

906

907

908

	Vapour pressure Sigma	B-c	Co	A-a	cn -/+
910	1	-	-	-	2
911	2	$C_{21}H_{44}-C_{24}H_{50}$	$C_{21}H_{44}-C_{22}H_{46}$	-	4
912	3	$C_{19}H_{40}-C_{23}H_{48}$	$C_{19}H_{40}-C_{21}H_{44}$	-	7
	4	$\leq C_{21}H_{44}$	$\leq C_{19}H_{40}$	-	9
	5	$\leq C_{20}H_{42}$	$\leq C_{17}H_{36}$	-	11

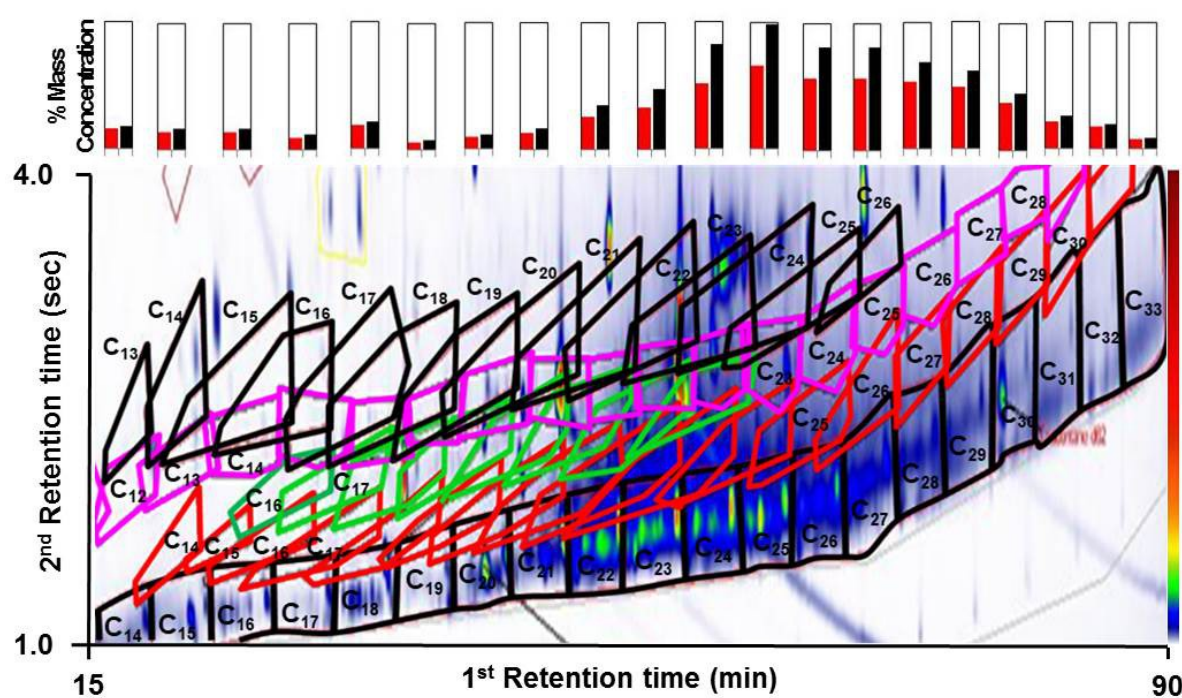
913

914

915 **Table 3.** Modal composition range and composition standard deviations, sigma, producing more
 916 realistic results that approximate REPARTEE-like behaviour. Vapour pressure parameterisation
 917 follows Myrdal and Yalkowski (1997; B-c in Figure 3), Compernolle et al. (2011; Co in Figure
 918 3), and Nannoolal et al., 2008; A-a in Figure 3). Column 'cn' indicates the carbon number of
 919 compounds n in the modal composition with a contribution bigger than 1%.

920

921



923

924

925 **Figure 1.** A GC \times GC chromatogram (bottom panel, contour plot) indicating homologous series of
 926 compounds identified in diesel engine exhaust emissions. Emissions from a light-duty diesel
 927 engine operating at 1800 revolutions per minute and 1.4 bar brake mean effective pressure.
 928 Compounds identified in the contour plot are indicated by the coloured polygons – Lower black
 929 polygons are n- + i-alkanes; red polygons are monocyclic alkanes; green polygons are bicyclic
 930 alkanes; pink polygons are aldehydes + ketones; and upper black polygons are monocyclic
 931 aromatics. Each peak in the contour plot represents a compound present in the emissions; warmer
 932 colours (e.g. red) are more intense peaks while colder colours (blue) are smaller peaks. Contour
 933 plot were produced by GC Image v2.5. Bar chart (top panel) show the volatility distribution of
 934 total alkanes (red) and total identified species (black), indicating that the majority of the
 935 emissions consist of alkanes. For details of the compound attribution method, see Alam et al.
 936 (2017).

937

938

939

940

69
70

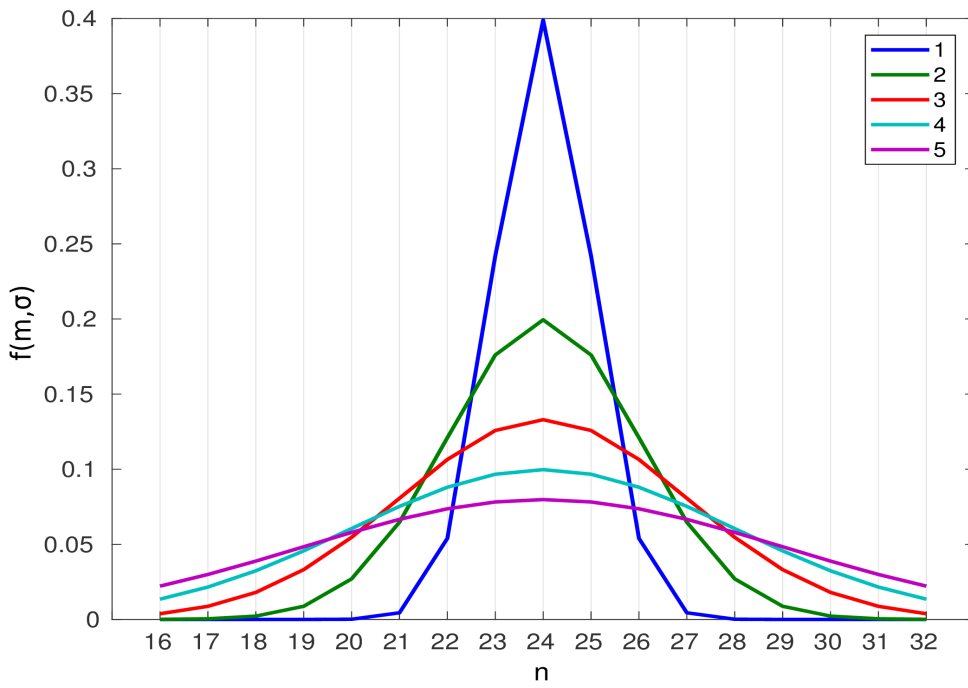


Figure 2. An example of nucleation mode UFP compositions, represented as mass fractions for surrogate compounds $C_nH_{(2n+2)}$, $n = [16:32]$, and described by a Gaussian distribution centred on $C_{24}H_{50}$ with standard deviation, σ , from 1 to 5.

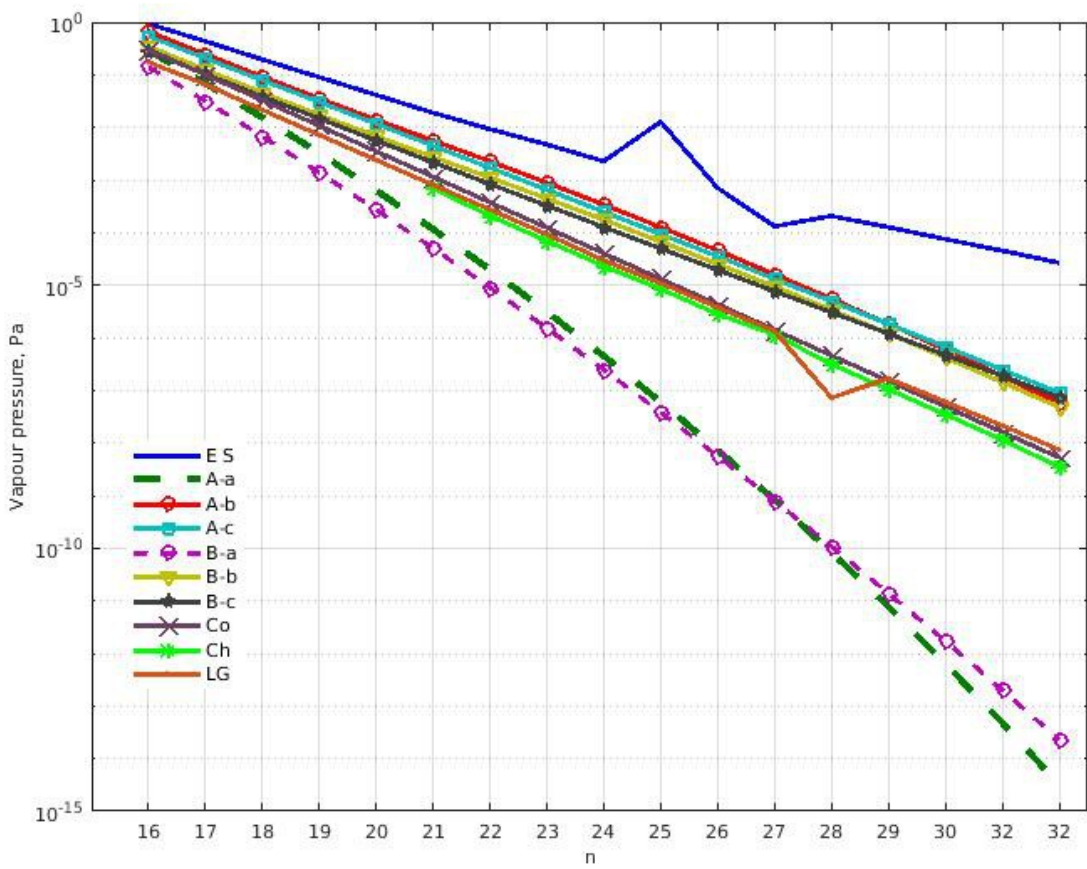


Figure 3. Vapour pressure data for selected n-alkanes $C_nH_{(2n+2)}$ where $n = [16:32]$ at 298K.

Abbreviations in the legend point to the source as follows: A and B refer to the vapour pressure data from Nannoolal et al. (2008) and Myrdal and Yalkowsky (1997), respectively; -a, -b and -c refer to the boiling point of Joback and Reid (1987), Stein and Brown (1994) and Nannoolal et al. (2004), respectively; ES refers to Epi Suite calculator (U.S. Environmental Protection Agency); Co to Compernolle et al. (2011); Ch to Chickos and Lipkind (2008); LG to Lemmon and Goodwin (2000).

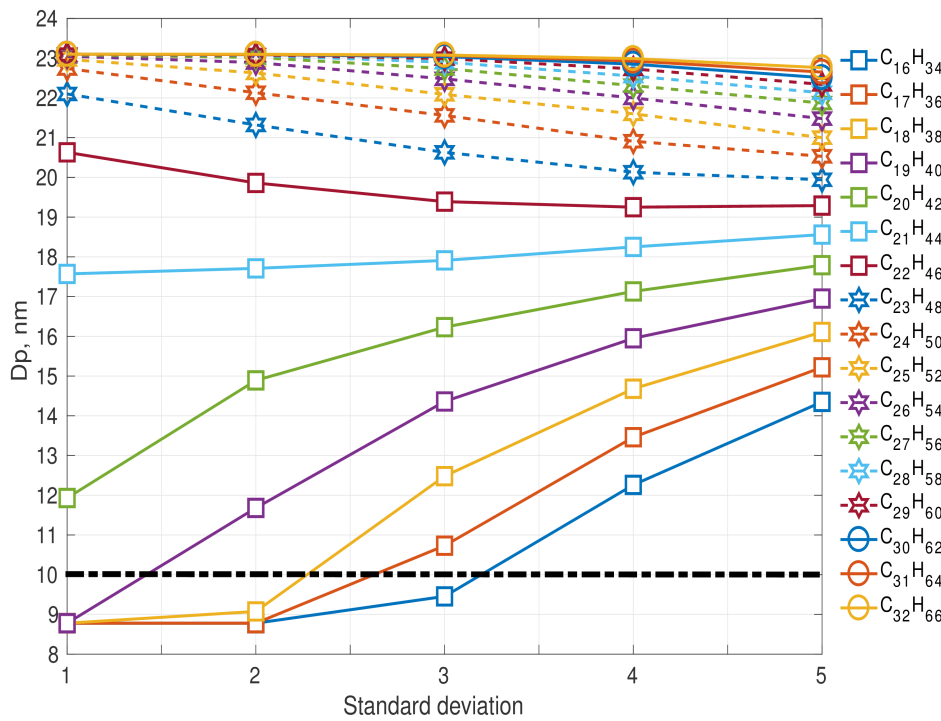


Figure 4. Nucleation mode peak diameter Dp [nm] at 1 s of simulation depending on the modal composition and the composition standard deviation. The initial nucleation mode peak diameter is at 23 nm (not shown on the figure). Vapour pressure data follows Compernolle et al. (2011).

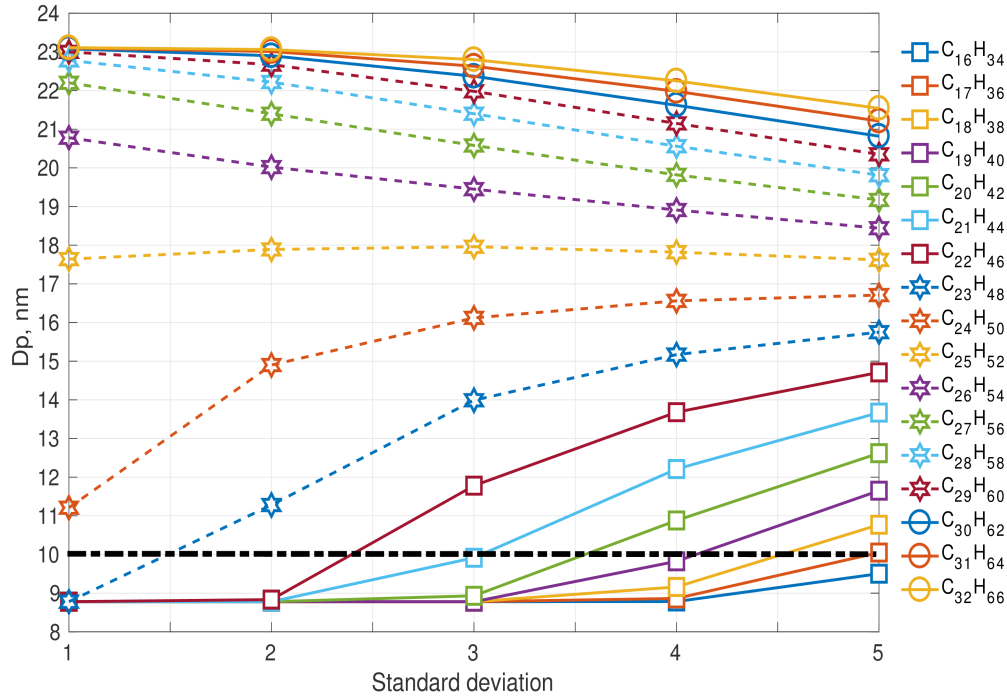


Figure 5. Nucleation mode peak diameter D_p [nm] at 100 s of simulation depending on the modal composition and the composition standard deviation. The initial nucleation mode peak diameter is at 23 nm (not shown on the figure). Vapour pressure data follows Compernolle et al. (2011).

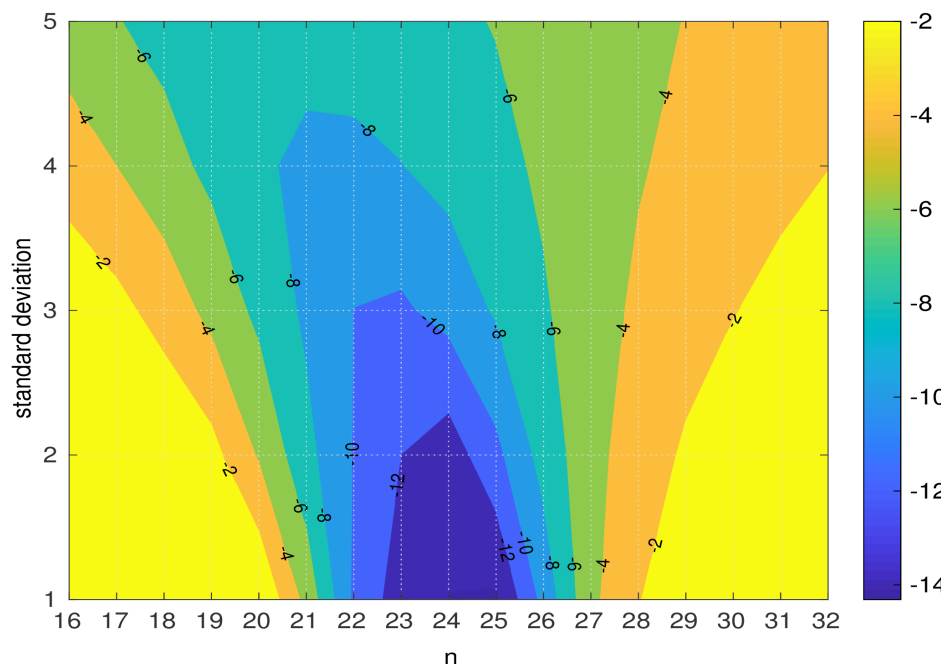


Figure 6. $D_{pg,nuc}$ difference between the nucleation mode peak diameter (nm) when using B-c vapour pressure and the nucleation mode peak diameter when using A-a vapour pressure for modal compositions $C_nH_{(2n+2)}$ where $n = [16:32]$.

1026
1027

1028

1029

1030

1031

1032

1033

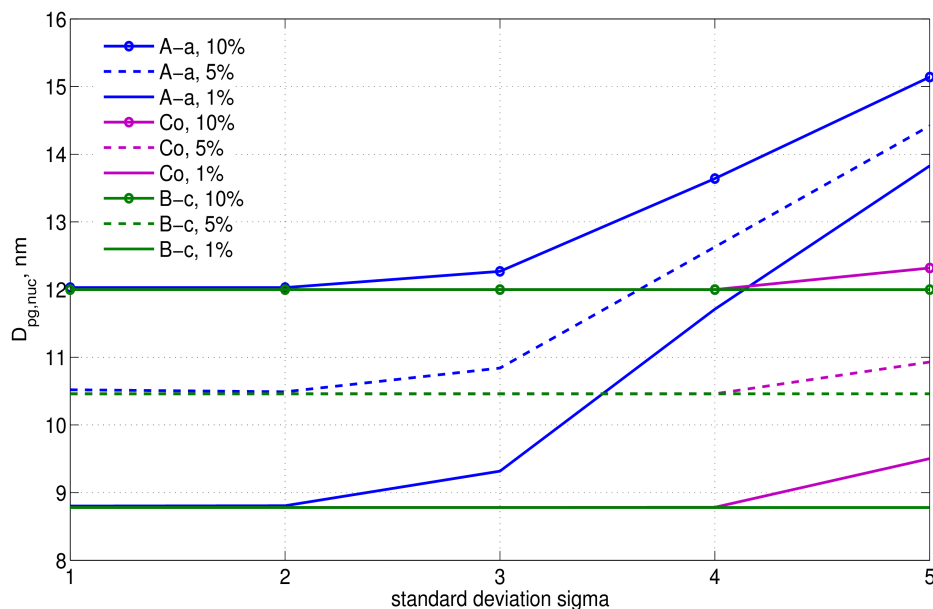
1034

1035

1036

1037

1038



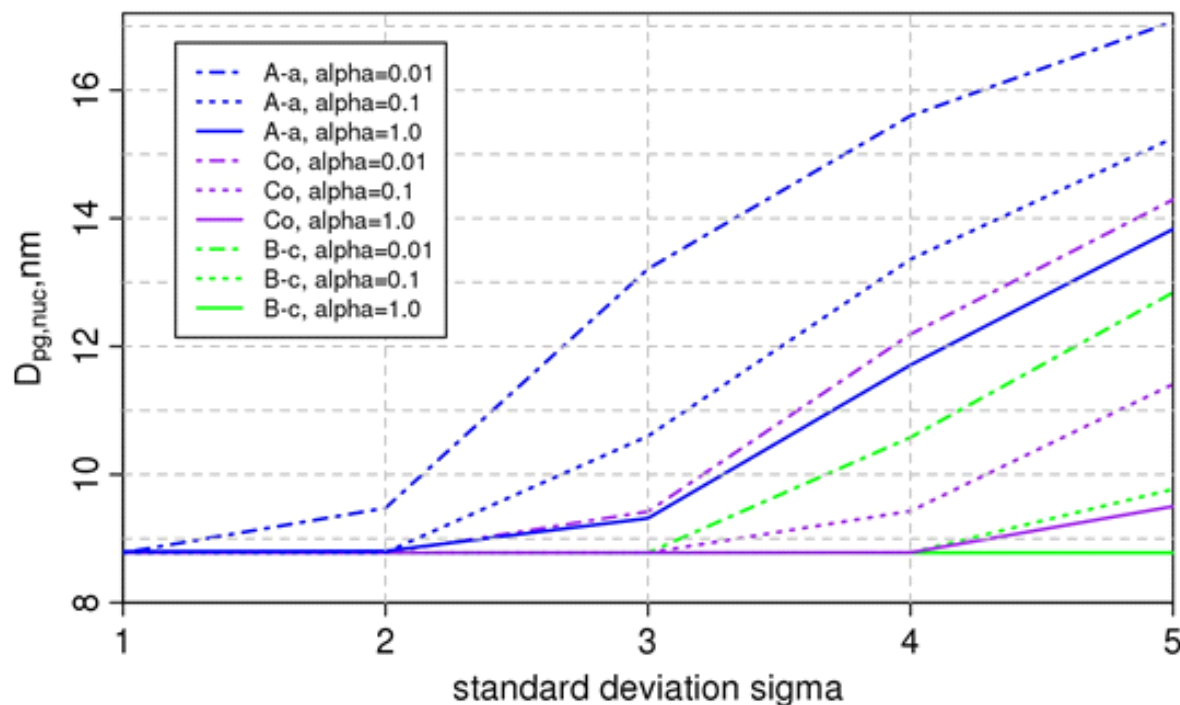
1039 **Figure 7.** Nucleation mode peak diameter D_p [nm] at 100 s: the ‘100-s effective non-volatile
1040 core’ for the nucleation mode. Results are shown at 1%, 5% and 10% initial non-volatile material
1041 in the nucleation mode particles, modal composition $C_{16}H_{34}$ and for various composition standard
1042 deviations.

1043

81
82

1044
1045

1046



1048 **Figure 8.** Nucleation mode peak diameter D_p [nm] at 100 s of simulation depending on the mass
1049 accommodation coefficient, the vapour pressure parameterisation, and the composition standard
1050 deviation. The initial nucleation mode peak diameter is at 23 nm (not shown on the figure).
1051 Results are shown for 1% initial non-volatile material in the nucleation mode particles, modal
1052 composition $C_{16}H_{34}$, and for various composition standard deviations. The vapour pressure
1053 parameterisations are labelled as for Figure 3.
1054

1056 **SUPPLEMENTARY MATERIAL**

1057

1058 **The influence of particle composition upon the evolution of**
1059 **urban ultrafine diesel particles on the neighbourhood scale**

1060

1061

1062 **Irina Nikolova, Xiaoming Cai, Mohammed Salim Alam,**
1063 **Soheil Zeraati-Rezaei, Jian Zhong, A. Rob MacKenzie and**
1064 **Roy M. Harrison**

1065

1066

1067 Here we present details of the input parameters used in the box model simulations (Section S1) and some results (Section S2). All figures and tables are given in the Appendix.

1069

1070 **S1. Model input parameters** - size distribution, vapour pressures, modal composition mass fractions in the nucleation
1071 and Aitken modes, gas-phase ambient concentrations.

1072

The initial size distribution is based on the measurements of Dall'Osto et al. (2011) and it is plotted in Figure 1-S. This ultrafine size resolved distribution represents the typical street canyon size distribution found next to a traffic site in Marylebone road in London (UK). The distribution has a well defined nucleation mode (particles with a diameter around or less than 30 nm) with a peak number concentration at $\sim 23 - 24$ nm. The Aitken mode (particles with diameter between 30 and 100 nm) is seen as a shoulder attached to the nucleation mode with a centre between 50 - 60 nm. Dall'Osto et al. (2011) show that the observed size distribution is subject to a major transformation caused by extensive evaporation of volatile material from the particles. The diameter of the nucleation mode particles decreased during the transport of the particles between the street canyon and the nearby city park over a distance of about 665m, as shown in Figure 1-S in the Appendix. The nucleation-mode peak diameter, $D_{pg,nuc}$, corresponding to the highest number concentration in the nucleation mode, was found at around 8 – 9 nm. In our study, we aim to put forward a realistic set of compositions and thermodynamic properties that could explain this diameter decrease as seen in the observations. Chemical analyses during the observations are missing; however, there are some laboratory data pointing to the nature of organics that participate in the composition from emitted particles collected from an engine testbed (Alam et al., 2016). Figure 2-S shows the normalised mass concentration per compound in the range $[C_{16}H_{34}:C_{32}H_{66}]$ for a given size class. Particles in the Nucleation and Aitken modes consist of about 10% and higher contribution from compounds in the range $C_{25}H_{52}-C_{29}H_{60}$.

1089

1090 In our modelling study the UFP size-re-
 1091 initialised as follows. The mass of a particle, $M_{ij} = \sum_{k=1}^2 \frac{\pi}{6} D p_i^3 \rho X_{jk} N_{ik}$ solved mass composition per mode (eq. 1) is
 1092 range [C₁₆H₃₄:C₃₂H₆₆] is expressed as M_{ij} , per size bin i and compound j in the
 (eq. 1)

1093 $i = 1, \dots, 15$ – number of size bins

1094 $j = 1 \dots 18$ - indices [1-17] corre

¹⁰⁹⁵ the inviolate core

1096 $k=1, 2$ - particle n

1007. D_{pi} = particle diameter per size bin i , m

1008 M_{\odot} size-resolved mass per size bin i at

1000 g m⁻³, particle density, held constant to avoid introducing bias.

1100 core.

1101 X_{jk} – fraction of mass in a particle in mode k per compound j

1102 $\pi = 3.14$

1103 and

1104 in which $n(Dp)$ is the differential size distribu- $N_{ik} = n(Dp)_{ik} \Delta Dp$ tion and N_{ik} is the number of particles per bin
1105 width ΔDp , [$\# \text{ m}^{-3}$]. The number log-normal size distribution (eq. 2) is given as follows:

1106

1107

$$n(Dp)_{ik} = \frac{N_k}{\sqrt{(2\pi)} Dp_i \ln(\sigma_{gk})} \exp\left(-0.5 \left(\frac{\ln(Dp_i/Dp_{gk})}{\ln(\sigma_{gk})}\right)^2\right) \quad (\text{eq. 2})$$

1108

1109

1110 $N_k = 3.0 \times 10^{10}$ and 1.8×10^{10} ($\# \text{ m}^{-3}$) are the total number concentrations in the Nucleation and Aitken mode, respectively

1111 $Dp_{gk} = 23$ and 65 nm are the geometric mean diameter in the Nucleation and Aitken mode, respectively

1112 $\sigma_{gk} = 1.6$ is the geometric standard deviation for both modes

1113 The fraction of mass X_{jk} of each particle in a mode k per compound SVOC in the range C₁₆H₃₄-C₃₂H₆₆ is calculated (eq. 3)

1114 as follows:

1115

$$X_{jk} = \frac{f(x_j | m_j, \sigma_{modal})}{\sum_{j=1}^{17} f(x_j | m_j, \sigma_{modal})} (xx_{jk} - sf_k) \quad (\text{eq. 3})$$

1116 where $f(x_j | m_j, \sigma_{modal})$ is the modal com- position in the form of a Gaussian dis-

1117 tribution (eq. 4), xx_{jk} is SVOC com- position given by the Gaussian para-

1118 meterisation (eq. 5), and sf_k is the solid involatile fraction per mode k :

1119

1120

$$f(x_j | m_j, \sigma_{modal}) = \frac{1}{\sqrt{(2\pi)} \sigma_{modal}} \exp\left(-0.5 \left(\frac{(x_j - m_j)}{\sigma_{modal}}\right)^2\right) \quad (\text{eq. 4})$$

1121

1122

$$xx_{jk} = \sum_{j=1}^{17} \frac{f(x_j | m_j, \sigma_{modal})}{\sum_{j=1}^{17} f(x_j | m_j, \sigma_{modal})} = 1 \quad 5$$

1123

1124 $\sigma_{modal} = 1, \dots, 5$ – standard deviation of modal composition

1125 $x_j = 1, \dots, 17$ – number assigned to the SVOC compound

1126 $m_j = 1, \dots, 17$ – modal composition compound for each SVOC in the range C₁₆H₃₄-C₃₂H₆₆

1127

1128 In this study the role of an involatile core (sf_k) is evaluated, too, by considering an involatile core to be 1%, 5% and 10%
1129 of the mass in a particle in the Nucleation mode ($k = 1$). Input modal composition mass fractions in the nucleation mode
1130 and composition standard deviation are presented in the Appendix in Table 1-S, 2-S and 3-S for involatile core of 1%,
1131 5% and 10%, respectively. The involatile core in the Aitken mode is 90% and the input modal composition mass frac-
1132 tions are given in Table 4-S in the Appendix.

1133

1134 Input vapour pressure parameterisations are given in Table 5-S. A-a, B-c and Co are used in this study to represent the
1135 uncertainties in the vapour pressure and evaluate the overall effect on the evaporative shrinkage of the nucleation mode

1136 particle diameter. Figure 3-S shows the ratio of vapour pressure between 298 K and 273 K for A-a, B-c and Co vapour
1137 pressure parameterisations and n-alkane compounds in the range C₁₆H₃₄-C₃₂H₆₆. The ratio for B-c and Co vapour pres-
1138 sure parameterisations is within an order of magnitude for compounds in the range C₁₆H₃₄-C₂₅H₅₂, however, it increases
1139 two to three orders of magnitude for higher molecular weight compounds. The ratio for A-a vapour pressure paramet-
1140 erisation is within an order of magnitude for compounds in the range C₁₆H₃₄-C₂₁H₄₄, and increases substantially for the
1141 remaining compounds. This would imply that for the selected timescale of 100 s there will be a shift in the threshold
1142 modal compositions to lower carbon-number compounds in comparison with the threshold modal compositions dis-
1143 cussed in this study. The temperature dependence on evaporation is not considered further in this study but should be
1144 borne in mind. The effect of changing the mass accommodation coefficient is discussed in section 3.4 of the main text.

1145

1146 The initial gas-phase concentrations for the n-alkanes in the range C₁₆H₃₄-C₃₂H₆₆ (Table 6-S) are as for the study in
1147 Nikolova et al. (2016) and are based on the roadside atmospheric measurements of Harrad et al. (2003).

1148

1149 S2. Results

1150 Figure 4-S and Figure 5-S show the nucleation mode peak diameter D_{pg,nuc} after 100 s using the vapour pressure para-
1151 meterisations following Myrdal-Yalkowsky et al (1997, B-c) and Nannoolal et al (2008, A-a), respectively. The nucle-
1152 ation mode particles consist of initial 1% non-volatile material. The threshold modal composition value changes from
1153 C₂₇H₅₆ for the B-c parameterisation (Figure 4-S) to C₂₂H₄₆ for A-a (Figure 5-S).

1154

1155 Figure 6-S shows the relative difference of the D_{pg,nuc} between the highest (B-c) and lowest (A-a) vapour pressure para-
1156 meterisations evaluated at 1 s, 10 s, 50 s and 100 s. Overall the largest difference is propagating to higher standard devi-
1157 ation sigma when simulation time increases as well as moving towards higher carbon-number modal compositions. In
1158 other words the relative differences become larger with time, pointing back to the huge differences in vapour pressure
1159 parameterisations between B-C and A-a. The choice of a particular vapour pressure dataset changes the range of carbon
1160 numbers by 2 in the first 10 seconds for which the highest relative difference is simulated. The 1-s relative difference is
1161 the highest for sigma 1 and modal compositions C₁₉H₄₀-C₂₁H₄₄. The 10-s highest relative difference has shifted to modal
1162 compositions C₂₁H₄₄-C₂₃H₄₈ and sigma = 1, 2. Higher relative differences (50% and more) are also simulated at sigma =
1163 3. The 100-s relative difference is the highest for modal compositions C₂₂H₄₆-C₂₄H₅₀ and sigma = 1, 2, 3, but also relat-
1164 ive differences of around 50% are simulated for sigma = 5.

1165

1166 Figure 7-S shows the ‘100-s effective involatile core’ for the nucleation mode particles. Results are shown at 1%, 5%
1167 and 10% initial non-volatile material in the nucleation mode particles, modal compositions C₂₄H₃₄ and C₃₂H₆₆ and for
1168 various composition standard deviations, sigma. Vapour pressure parameterisations follow Myrdal and Yalkowski
1169 (1997; B-c in Table 1-S) and Nannoolal et al. (2008; A-a in Table 1-S). Figure 5-S presents the sensitivity to the non-

91

92

1170 volatile core in the nucleation mode for modal compositions C₂₄H₅₀ and C₃₂H₆₆ evaluated for B-c and A-a vapour pres-
1171 sure parameterisations. The 100-s effective involatile core for modal composition C₂₄H₅₀ and B-c vapour pressure para-
1172 meterisation increases when the non-volatile core increases. This is simulated for an increasing σ too, due the increasing
1173 number of lower volatility components that are added into the particle composition. The 100-s effective involatile core
1174 for modal compositions C₂₄H₅₀ (for A-a vapour pressure) and C₃₂H₆₆ (for A-a and B-c vapour pressures) shows an op-
1175 posite trend with respect to sigma, i.e., the 100-s effective involatile core decreases due to the increasing number of
1176 higher volatility components added into the particle composition.

1177

1178 Figure 8-S shows the nucleation mode peak diameter D_{pg,nuc} after 100 s for different values of the mass accommodation
1179 coefficient (α), modal composition, and composition standard deviation (σ), using the vapour pressure parameterisa-
1180 tions following Myrdal-Yalkowsky et al (1997, B-c) and Nannoolal et al (2008, A-a), respectively. The nucleation
1181 mode particles consist of initial 1% non-volatile material and modal composition C₂₄H₅₀ and C₃₂H₆₆, i.e. less volatile
1182 compositions that shown in Figure 8 of the main text. A wide range of D_{pg,nuc} can result from different values of α and σ
1183 for a modal composition of C₂₄H₅₀ and the B-c vapour pressure parameterisation (see main text Figure 3 for vapour
1184 pressure nomenclature). For the other combinations of modal composition and vapour pressure parameterisation shown,
1185 the choice of α has little effect on the model results.

1186

1187

1188 Acknowledgements

1189 This work is part of the FASTER project, ERC-2012-AdG, Proposal No. 320821 sponsored by the European Research
1190 Council (ERC).

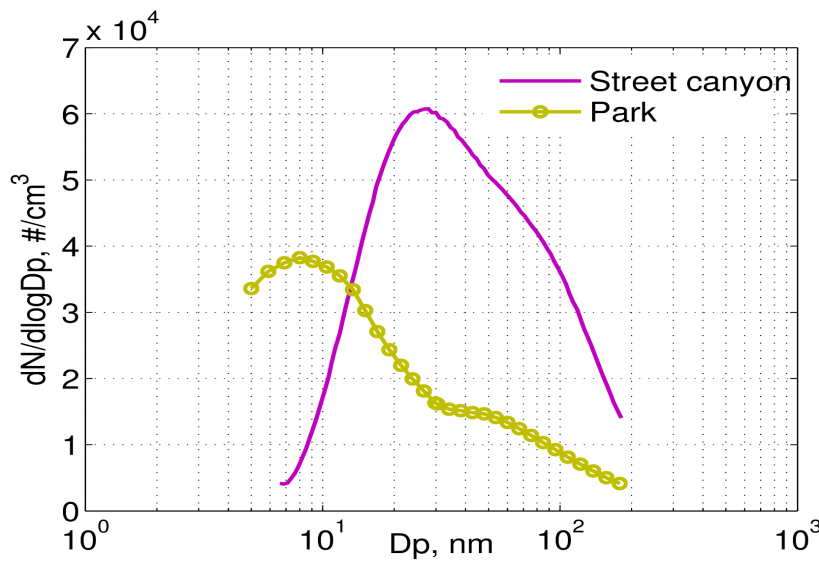
1191

1192 References

- 1193
- 1194 Alam, M. S, Rezaei, S. Z., Stark, C. P., Liang, Z., Xu, H. M., Harrison, R. M.: The character-
1195 isation of diesel exhaust particles – composition, size distribution and partitioning, Faraday
1196 Discuss., 189, 69-84, 2016.
- 1197 Chickos, J., Lipkind, D.: Hypothetical thermodynamic properties: vapour pressures and vaporization enthalpies of the
1198 even n-Alkanes from C₇₈ to C₉₂ at T= 298.15K by correlation-gas chromatography, J. Chem. Eng. Data, 53, 2432-
1200 2440, 2008.
- 1201 Compernolle, S., Ceulemans, K., Muller, J. -F.: EVAPORATION: a new vapour pressure estimation method for organic
1202 molecules including non-additivity and intramolecular interactions, Atmos. Chem. Phys., 11, 9431-9450, 2011.
- 1203
- 1204 Dall'Osto, M., Thorpe, A., Beddows, D.C.S., Harrison, R.M., Barlow, J.F., Dunbar, T., Williams, P.I., Coe, H.: Re-
1205 markable dynamics of nanoparticles in the urban atmosphere, Atmos. Chem. Phys., 11, 6623-6637, 2011.
- 1206
- 1207 Joback, K., Reid, R.: Estimation of pure-component properties from group-contributions, Chem. Eng. Commun., 57,
1208 233-243, 1987.
- 1209
- 1210

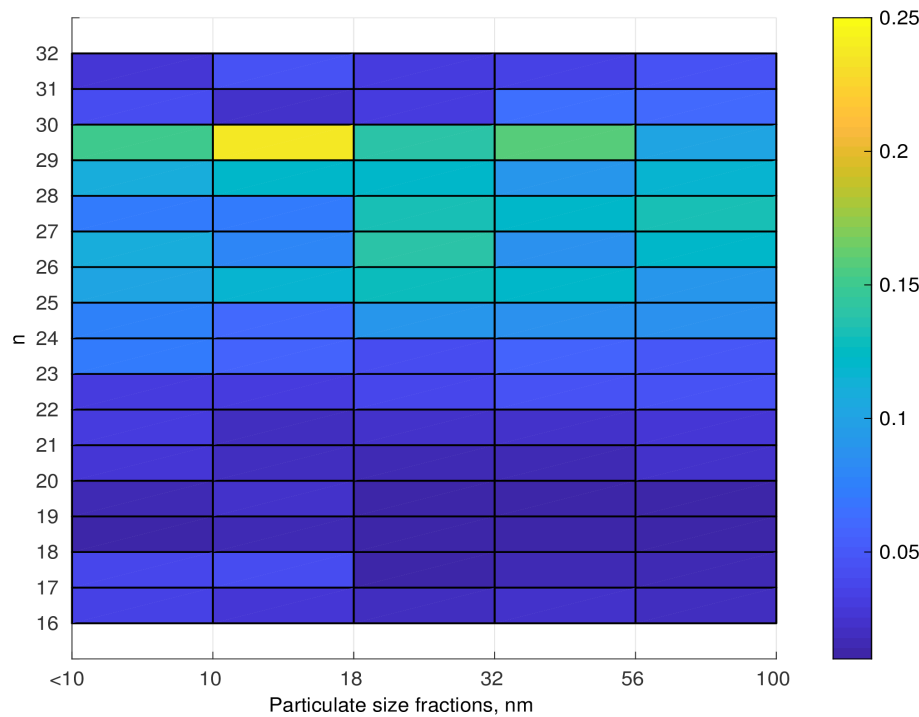
- 1211 Harrad, S., Hassoun, S., Callen Romero, M. S., Harrison, R. M.: Characterisation and source attribution of the semi-
1212 volatile organic content of atmospheric particles and associate
1213 vapour phase in Birmingham, UK , Atmos. Environ., 37, 4985-4991, 2003.
1214
- 1215 Myrdal, P. B., Yalkowsky, S. H.: Estimating pure component vapor pressures of complex organic molecules, Ind. Eng.
1216 Chem. Res., 36, 2494-2499, 1997.
1217
- 1218 Nannooolal, Y., Rarey, J., Ramjugernath, D., Cordes, W.: Estimation of pure component properties: Part 1. Estimation
1219 of the normal boiling point of non-electrolyte organic compounds via
1220 group contributions and group interactions, Fluid Phase Equilibr., 226, 45-63, 2004.
1221
- 1222 Nannooolal, Y., Rarey, J., Ramjugernath, D.: Estimation of pure component properties: Part 3. Estimation of the vapor
1223 pressure of non-electrolyte organic compounds via group contributions and group interactions, Fluid Phase Equilibr.,
1224 269, 117-133, 2008.
1225
- 1226 Nikolova, I., MacKenzie, A. R., Cai, X., Alam, M. S., Harrison, R. M.: Modelling component evaporation and coposi-
1227 tion change of traffic-induced ultrafine particles during travel from street canyon to urban background, Faraday Dis-
1228 cuss., 189, 529-46, 2016.
1229
- 1230 Stein, S. E., Brown, R. L.: Estimation of normal boiling points from group contributions, J. Chem. Inf. Comp. Sci., 34,
1231 581-587, 1994.
1232
- 1233
- 1234 Topping, D., Barley, M., Bane, M. K., Higham, N., Aumont, B., Dingle, N., McFiggans, G.: UManSysProp v1.0: an
1235 online and open-source facility for molecular property prediction and atmospheric aerosol calculations, Geosci. Model
1236 Dev., 9, 899-914, 2016.
1237

1238

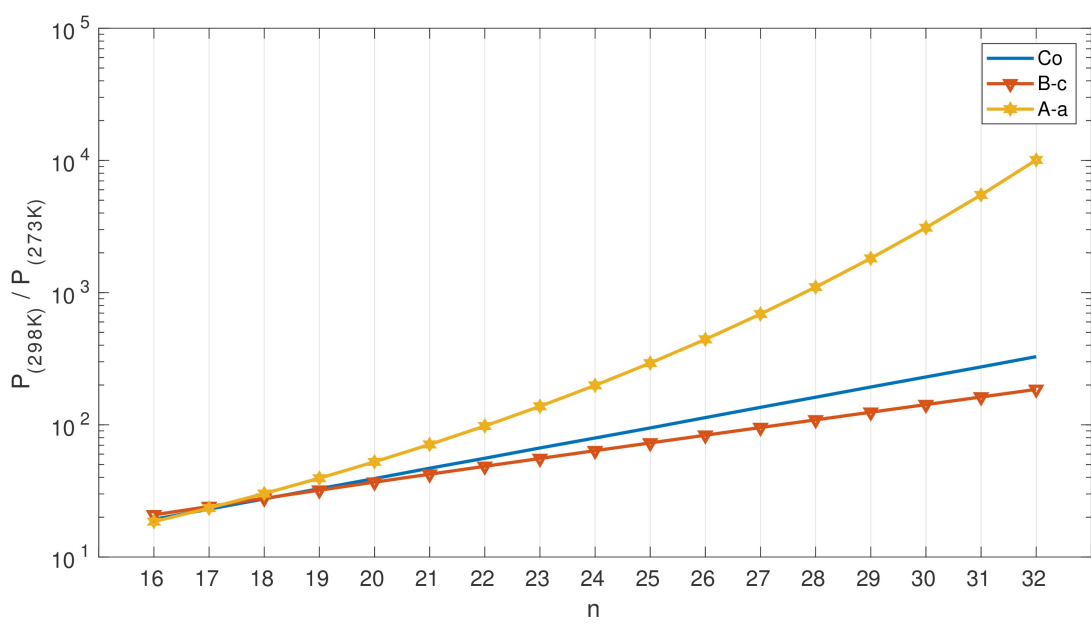


1240

1241 *Figure 1-S. Measured ultrafine particle size distribution in a street canyon (Marylebone Road, London, UK) and the*
 1242 *nearby city park (Regents Park, London, UK).*



1244 *Figure 2-S. Laboratory particulate mass fractions of n-alkanes $C_nH_{(2n+2)}$, where $n=[16:32]$ for selected particulate dia-*
 1245 *meter range [$<10:100$ nm]. Figure plotted based on the data presented in Alam et al. (2016).*



1246 *Figure 3-S. Vapour pressure ratios for vapour pressure parameterisations A-a, B-c and Co and n-alkane compounds*
1247 $C_nH_{(2n+2)}$, $n=[16:32]$, between 298 K and 273 K.

1248

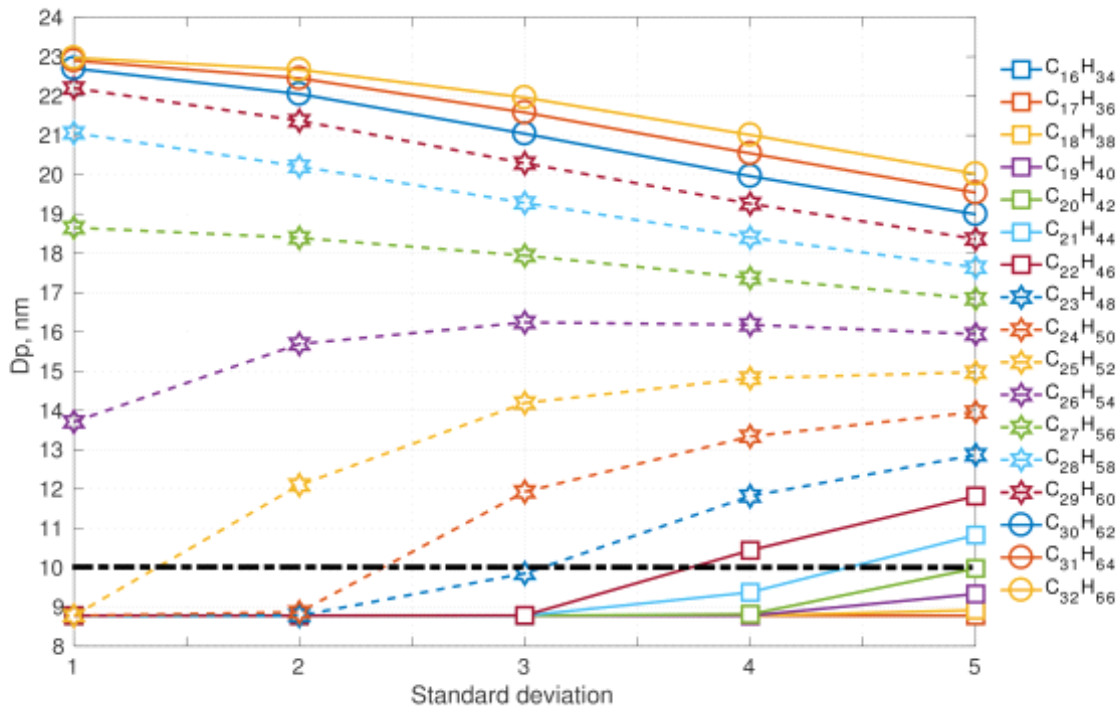


Figure 4-S. Nucleation mode peak diameter Dp [nm] at 100 s of simulation depending on the modal composition and the composition standard deviation. The initial nucleation mode peak diameter is at 23 nm (not shown on the figure). Vapour pressure data follows Myrdal Yalkowsky et al. (1997, B-c). Initial nucleation mode particle involatile core is 1%.

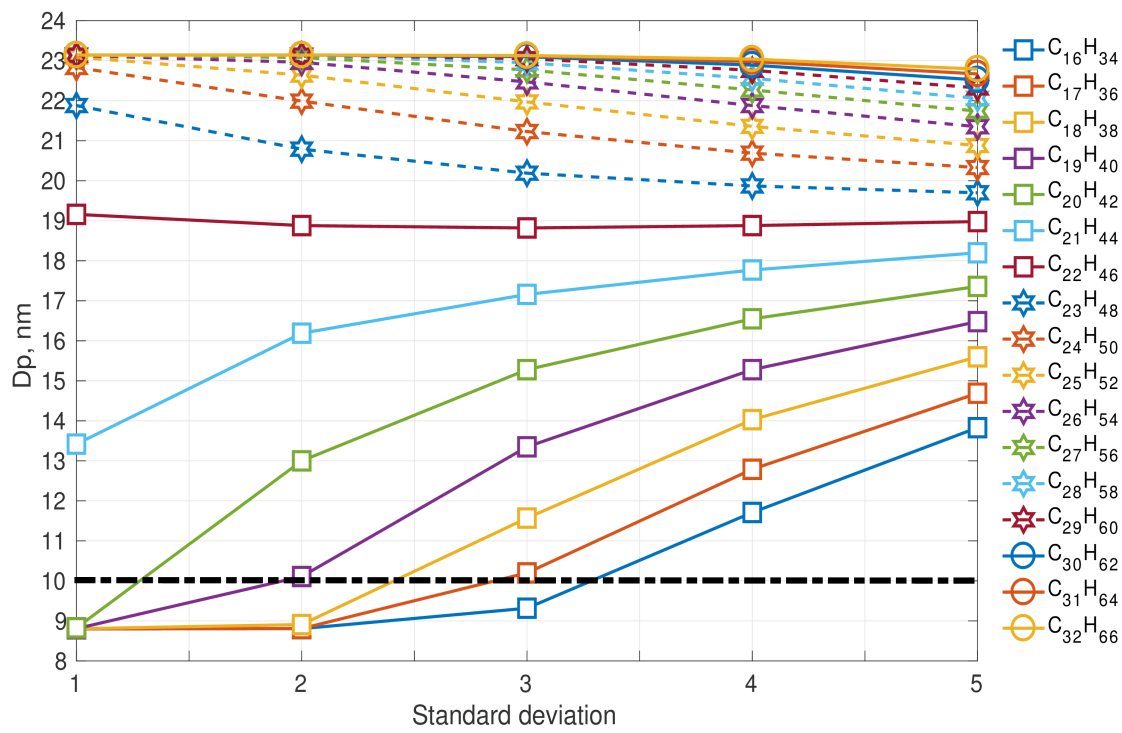
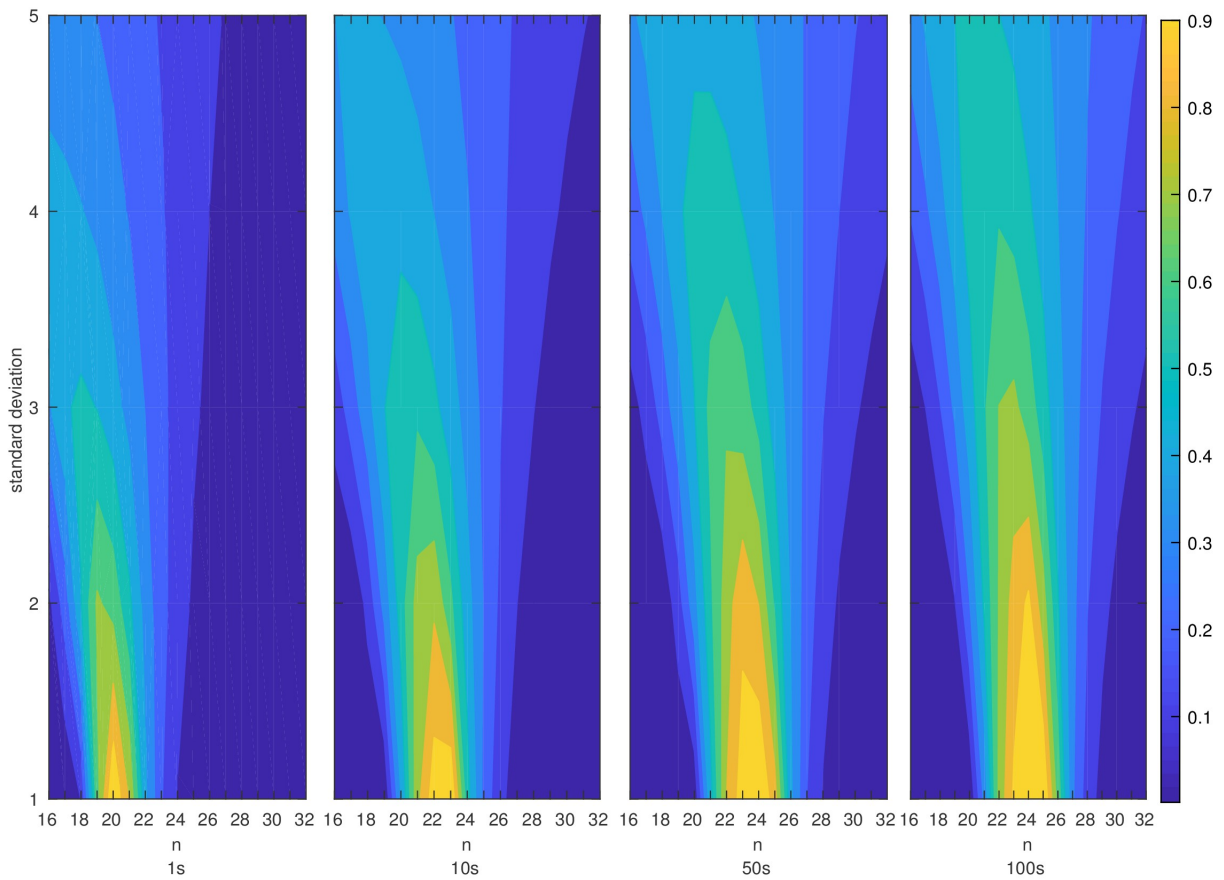
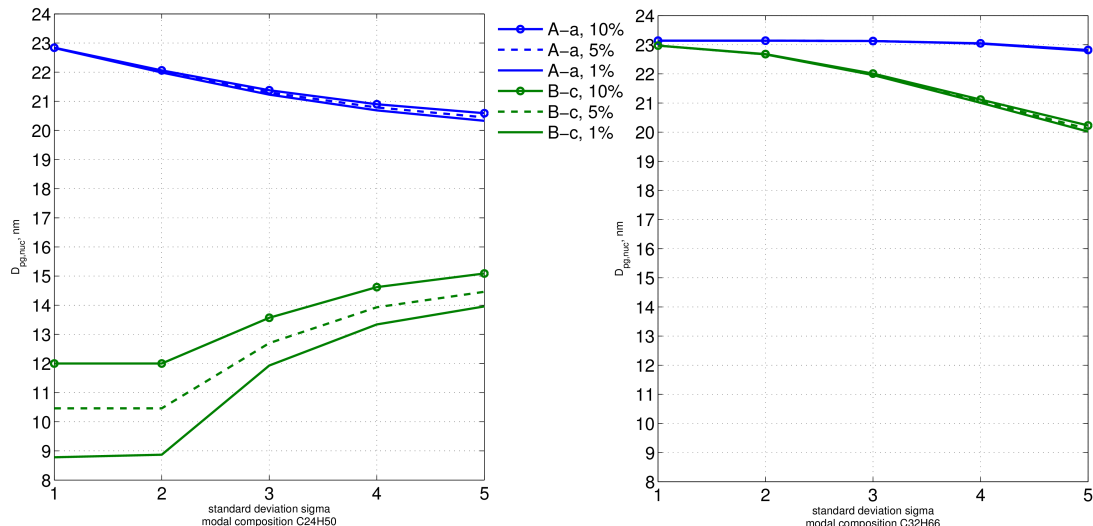


Figure 5-S. Nucleation mode peak diameter D_p [nm] at 100 s of simulation depending on the modal composition and the composition standard deviation. The initial nucleation mode peak diameter is at 23 nm (not shown on the figure). Vapour pressure data follows Nannoolal et al. (2008, A-a). Initial nucleation mode particle involatile core is 1%.

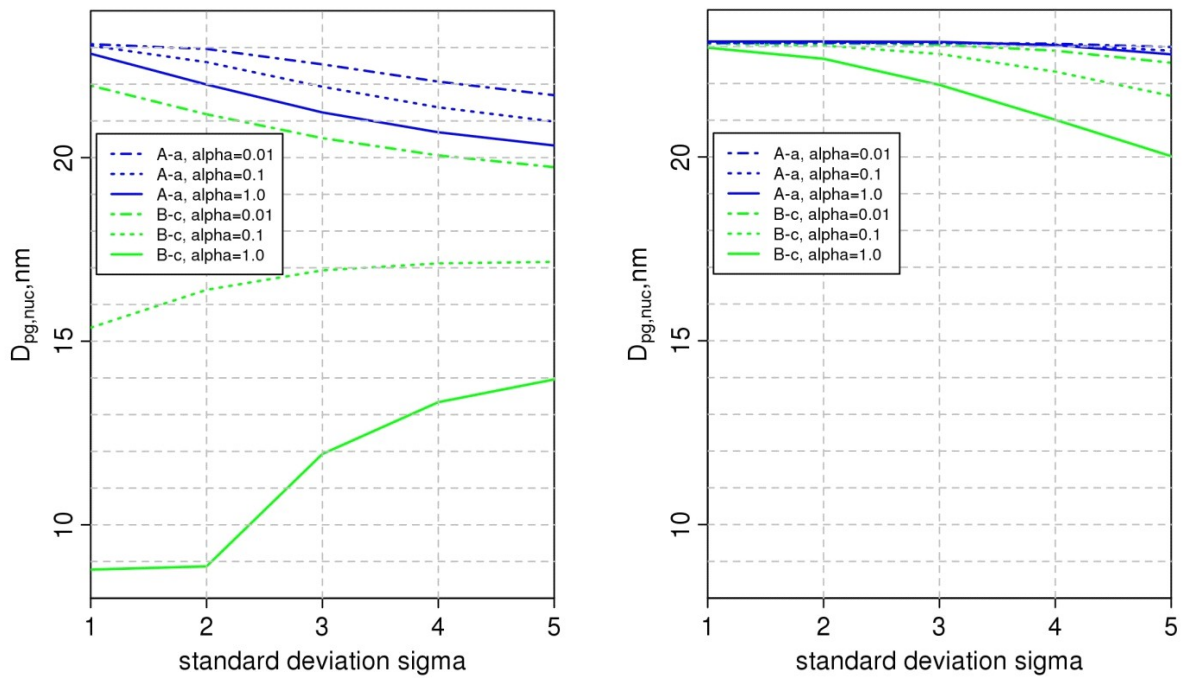


1250 *Figure 6-S. Nucleation mode peak diameter relative difference (in %) between B-c and A-a vapour pressure paramet-*
 1251 *erisations for modal compositions $C_nH_{(2n+2)}$ for $n = 16:32$ and composition standard deviation from 1 to 5.*
 1252

1253



1254 *Figure 7-S. Nucleation mode peak diameter D_p [nm] after 100s: the '100-s effective involatile core' for the nucleation*
 1255 *mode. Results are shown at 1%, 5% and 10% initial non-volatile material in the nucleation mode particles, modal com-*
 1256 *positions $C_{24}H_{50}$ (left) and $C_{32}H_{66}$ (right) and for various composition standard deviations, sigma. Vapour pressure*
 1257 *parameterisation follows Myrdal and Yalkowski (1997; B-c in Table I-S) and Nannoolal et al. (2008; A-a in Table I-*
 1258 *S).*



1261 *Figure 8-S. Nucleation mode peak diameter D_p [nm] at 100 s of simulation depending on the mass accommodation*
 1262 *coefficient, the vapour pressure parameterisation, and the composition standard deviation. Results are shown at ac-*
 1263 *commodation coefficients of 0.01, 0.1 and 1.0, modal compositions $C_{24}H_{50}$ (left) and $C_{32}H_{66}$ (right) and for various com-*
 1264 *position standard deviations, sigma. Vapour pressure parameterisation follows Myrdal and Yalkowski (1997; B-c in*
 1265 *Table 1-S) and Nannoolal et al. (2008; A-a in Table 1-S).*

1266

σ	modal composition																				
1	$C_{10}H_{34}$	$C_{11}H_{36}$	$C_{12}H_{36}$	$C_{13}H_{40}$	$C_{14}H_{40}$	$C_{15}H_{40}$	$C_{16}H_{40}$	$C_{17}H_{44}$	$C_{18}H_{44}$	$C_{19}H_{48}$	$C_{20}H_{48}$	$C_{21}H_{48}$	$C_{22}H_{48}$	$C_{23}H_{50}$	$C_{24}H_{50}$	$C_{25}H_{54}$	$C_{26}H_{54}$	$C_{27}H_{58}$	$C_{28}H_{58}$	$C_{29}H_{60}$	$C_{30}H_{60}$
2	$C_{10}H_{34}$	$C_{11}H_{36}$	$C_{12}H_{36}$	$C_{13}H_{40}$	$C_{14}H_{40}$	$C_{15}H_{40}$	$C_{16}H_{40}$	$C_{17}H_{44}$	$C_{18}H_{44}$	$C_{19}H_{48}$	$C_{20}H_{48}$	$C_{21}H_{48}$	$C_{22}H_{48}$	$C_{23}H_{50}$	$C_{24}H_{50}$	$C_{25}H_{54}$	$C_{26}H_{54}$	$C_{27}H_{58}$	$C_{28}H_{58}$	$C_{29}H_{60}$	$C_{30}H_{60}$
3	$C_{10}H_{34}$	$C_{11}H_{36}$	$C_{12}H_{36}$	$C_{13}H_{40}$	$C_{14}H_{40}$	$C_{15}H_{40}$	$C_{16}H_{40}$	$C_{17}H_{44}$	$C_{18}H_{44}$	$C_{19}H_{48}$	$C_{20}H_{48}$	$C_{21}H_{48}$	$C_{22}H_{48}$	$C_{23}H_{50}$	$C_{24}H_{50}$	$C_{25}H_{54}$	$C_{26}H_{54}$	$C_{27}H_{58}$	$C_{28}H_{58}$	$C_{29}H_{60}$	$C_{30}H_{60}$
4	$C_{10}H_{34}$	$C_{11}H_{36}$	$C_{12}H_{36}$	$C_{13}H_{40}$	$C_{14}H_{40}$	$C_{15}H_{40}$	$C_{16}H_{40}$	$C_{17}H_{44}$	$C_{18}H_{44}$	$C_{19}H_{48}$	$C_{20}H_{48}$	$C_{21}H_{48}$	$C_{22}H_{48}$	$C_{23}H_{50}$	$C_{24}H_{50}$	$C_{25}H_{54}$	$C_{26}H_{54}$	$C_{27}H_{58}$	$C_{28}H_{58}$	$C_{29}H_{60}$	$C_{30}H_{60}$
5	$C_{10}H_{34}$	$C_{11}H_{36}$	$C_{12}H_{36}$	$C_{13}H_{40}$	$C_{14}H_{40}$	$C_{15}H_{40}$	$C_{16}H_{40}$	$C_{17}H_{44}$	$C_{18}H_{44}$	$C_{19}H_{48}$	$C_{20}H_{48}$	$C_{21}H_{48}$	$C_{22}H_{48}$	$C_{23}H_{50}$	$C_{24}H_{50}$	$C_{25}H_{54}$	$C_{26}H_{54}$	$C_{27}H_{58}$	$C_{28}H_{58}$	$C_{29}H_{60}$	$C_{30}H_{60}$

1269 Table 1-S. Input modal composition mass fractions (by columns) in the nucleation mode and composition standard deviation for involatile core of 1%.

1270

1271

		modal composition																			
	σ	$C_{10}H_{34}$	$C_{17}H_{36}$	$C_{18}H_{38}$	$C_{19}H_{40}$	$C_{20}H_{42}$	$C_{21}H_{44}$	$C_{22}H_{46}$	$C_{23}H_{48}$	$C_{24}H_{50}$	$C_{25}H_{52}$	$C_{26}H_{54}$	$C_{27}H_{56}$	$C_{28}H_{58}$	$C_{29}H_{60}$	$C_{30}H_{62}$	$C_{31}H_{64}$	$C_{32}H_{66}$			
1	5.42E-01	2.44E-01	5.15E-02	4.21E-03	1.27E-04	1.41E-06	5.77E-09	8.68E-12	4.80E-15	9.77E-19	7.31E-23	2.01E-27	2.04E-32	7.60E-38	1.05E-43	5.58E-50	1.39E-56				
	3.29E-01	4.03E-01	2.31E-01	5.13E-02	4.21E-03	1.27E-04	1.41E-06	5.77E-09	8.68E-12	4.80E-15	9.77E-19	7.31E-23	2.01E-27	2.04E-32	7.63E-38	1.11E-43	7.51E-50				
	7.33E-02	2.44E-01	3.81E-01	2.30E-01	5.13E-02	4.21E-03	1.27E-04	1.41E-06	5.77E-09	8.68E-12	4.80E-15	9.77E-19	7.31E-23	2.01E-27	2.05E-32	8.07E-38	1.49E-43				
	6.02E-03	5.45E-02	2.31E-01	3.79E-01	2.30E-01	5.13E-02	4.21E-03	1.27E-04	1.41E-06	5.77E-09	8.68E-12	4.80E-15	9.77E-19	7.31E-23	2.02E-27	2.17E-32	1.09E-37				
	1.82E-04	4.47E-03	5.15E-02	2.30E-01	3.79E-01	2.30E-01	5.13E-02	4.21E-03	1.27E-04	1.41E-06	5.77E-09	8.68E-12	4.80E-15	9.77E-19	7.34E-23	2.14E-27	2.92E-32				
	2.02E-06	1.35E-04	4.23E-03	5.13E-02	2.30E-01	3.79E-01	2.30E-01	5.13E-02	4.21E-03	1.27E-04	1.41E-06	5.77E-09	8.68E-12	4.80E-15	9.81E-19	7.76E-23	2.88E-27				
	8.26E-09	1.50E-06	1.28E-04	4.21E-03	5.13E-02	2.30E-01	3.79E-01	2.30E-01	5.13E-02	4.21E-03	1.27E-04	1.41E-06	5.77E-09	8.68E-12	4.82E-15	1.04E-18	1.05E-22				
	1.24E-11	6.13E-09	1.42E-06	1.27E-04	4.21E-03	5.13E-02	2.30E-01	3.79E-01	2.30E-01	5.13E-02	4.21E-03	1.27E-04	1.41E-06	5.77E-09	8.72E-12	5.10E-15	1.40E-18				
	6.86E-15	9.22E-12	5.80E-09	1.41E-06	1.27E-04	4.21E-03	5.13E-02	2.30E-01	3.79E-01	2.30E-01	5.13E-02	4.21E-03	1.27E-04	1.41E-06	5.80E-09	9.22E-12	6.86E-15				
	1.40E-18	5.10E-15	8.72E-12	5.77E-09	1.41E-06	1.27E-04	4.21E-03	5.13E-02	2.30E-01	3.79E-01	2.30E-01	5.13E-02	4.21E-03	1.27E-04	1.42E-06	6.13E-09	1.24E-11				
	1.05E-22	1.04E-18	4.82E-15	8.68E-12	5.77E-09	1.41E-06	1.27E-04	4.21E-03	5.13E-02	2.30E-01	3.79E-01	2.30E-01	5.13E-02	4.21E-03	1.28E-04	1.50E-06	8.25E-09				
	2.88E-27	7.76E-27	9.81E-19	4.80E-15	8.68E-12	5.77E-09	1.41E-06	1.27E-04	4.21E-03	5.13E-02	2.30E-01	3.79E-01	2.30E-01	5.13E-02	4.21E-03	1.35E-04	2.02E-06				
	2.92E-32	2.14E-27	7.34E-23	9.77E-19	4.80E-15	8.68E-12	5.77E-09	1.41E-06	1.27E-04	4.21E-03	5.13E-02	2.30E-01	3.79E-01	2.30E-01	5.15E-02	4.47E-03	1.82E-04				
	1.09E-37	2.17E-32	2.02E-27	7.31E-23	9.77E-19	4.80E-15	8.68E-12	5.77E-09	1.41E-06	1.27E-04	4.21E-03	5.13E-02	2.30E-01	3.79E-01	2.30E-01	5.13E-02	4.21E-03	1.31E-04	6.02E-03		
	1.49E-43	8.07E-38	2.05E-32	2.01E-27	7.31E-23	9.77E-19	4.80E-15	8.68E-12	5.77E-09	1.41E-06	1.27E-04	4.21E-03	5.13E-02	2.30E-01	3.81E-01	2.44E-01	7.33E-02				
	7.51E-50	1.11E-43	7.63E-38	2.04E-32	2.01E-27	7.31E-23	9.77E-19	4.80E-15	8.68E-12	5.77E-09	1.41E-06	1.27E-04	4.21E-03	5.13E-02	2.31E-01	4.03E-01	3.29E-01				
	1.39E-56	5.58E-50	1.05E-43	7.60E-38	2.04E-32	2.01E-27	7.31E-23	9.77E-19	4.80E-15	8.68E-12	5.77E-09	1.41E-06	1.27E-04	4.21E-03	5.15E-02	2.44E-01	5.42E-01				
2	$C_{10}H_{34}$	$C_{17}H_{36}$	$C_{18}H_{38}$	$C_{19}H_{40}$	$C_{20}H_{42}$	$C_{21}H_{44}$	$C_{22}H_{46}$	$C_{23}H_{48}$	$C_{24}H_{50}$	$C_{25}H_{52}$	$C_{26}H_{54}$	$C_{27}H_{56}$	$C_{28}H_{58}$	$C_{29}H_{60}$	$C_{30}H_{62}$	$C_{31}H_{64}$	$C_{32}H_{66}$				
	3.16E-01	2.16E-01	1.28E-01	6.40E-02	2.59E-02	8.35E-03	2.11E-03	4.15E-04	6.36E-05	7.59E-06	7.07E-07	5.13E-08	2.92E-09	1.32E-10	4.84E-12	1.49E-13	4.00E-15				
	2.79E-01	2.44E-01	1.86E-01	1.20E-01	6.22E-02	2.57E-02	8.33E-03	2.11E-03	4.15E-04	6.36E-05	7.60E-06	7.08E-07	5.18E-08	3.00E-09	1.41E-10	5.59E-12	1.93E-13				
	1.92E-01	2.16E-01	1.21E-01	1.74E-01	1.16E-01	6.17E-02	2.57E-02	8.33E-03	2.11E-03	4.15E-04	6.36E-05	7.61E-06	7.14E-07	5.32E-08	3.22E-09	1.63E-10	7.23E-12				
	1.03E-01	1.48E-01	1.86E-01	1.97E-01	1.69E-01	6.15E-02	2.56E-02	8.33E-03	2.11E-03	4.15E-04	6.37E-05	7.68E-06	7.34E-07	5.70E-08	3.72E-09	2.11E-10					
	4.28E-02	7.93E-02	1.28E-01	1.74E-01	1.92E-01	1.68E-01	6.15E-02	2.56E-02	8.33E-03	2.11E-03	4.16E-04	6.43E-05	7.90E-06	7.87E-07	6.59E-08	4.81E-09					
	1.39E-02	3.31E-02	6.86E-02	1.20E-01	1.69E-01	1.90E-01	1.67E-01	6.15E-02	2.56E-02	8.33E-03	2.11E-03	4.19E-04	6.61E-05	8.47E-06	9.10E-07						
	3.51E-03	1.07E-02	2.86E-02	6.40E-02	1.61E-01	1.68E-01	1.90E-01	1.67E-01	6.15E-02	2.57E-02	8.35E-03	2.13E-03	4.31E-04	7.09E-05	9.79E-06	1.18E-06					
	6.91E-04	2.71E-03	9.28E-02	6.22E-02	1.65E-01	1.67E-01	1.67E-01	6.16E-02	2.57E-02	8.42E-03	2.19E-03	4.62E-04	8.19E-05	1.27E-05							
	1.06E-04	5.34E-04	2.35E-03	8.66E-03	2.59E-02	6.17E-02	1.15E-01	1.67E-01	1.90E-01	1.67E-01	1.15E-01	6.16E-02	2.57E-02	8.66E-03	2.35E-03	5.34E-04	1.06E-04				
	1.27E-05	8.19E-05	4.62E-04	2.19E-03	8.42E-03	2.57E-02	6.16E-02	1.15E-01	1.67E-01	1.90E-01	1.67E-01	1.15E-01	6.22E-02	2.67E-02	9.28E-03	2.71E-03	6.91E-04				
	1.18E-06	9.79E-06	7.09E-05	4.31E-04	2.13E-03	8.35E-03	2.57E-02	6.15E-02	1.15E-01	1.67E-01	1.90E-01	1.68E-01	1.16E-01	6.40E-02	2.86E-02	1.07E-02	3.51E-03				
	8.53E-08	9.10E-07	4.87E-06	6.61E-05	4.19E-04	2.11E-03	8.33E-03	2.56E-02	6.15E-02	1.15E-01	1.67E-01	1.90E-01	1.69E-01	1.20E-01	6.86E-02	3.31E-02	1.39E-02				
	4.81E-09	6.59E-08	7.87E-07	7.90E-06	6.43E-05	4.16E-04	2.11E-03	8.33E-03	2.56E-02	6.15E-02	1.15E-01	1.68E-01	1.92E-01	1.74E-01	1.28E-01	7.93E-02	4.28E-02				
	2.11E-10	3.72E-09	5.70E-08	7.34E-07	7.68E-06	6.37E-05	4.15E-04	2.11E-03	8.33E-03	2.56E-02	6.16E-02	1.15E-01	1.68E-01	1.92E-01	1.74E-01	1.30E-01	7.05E-02				
	7.23E-12	1.63E-10	3.22E-09	5.32E-08	7.14E-07	7.61E-06	6.36E-05	4.15E-04	2.11E-03	8.33E-03	2.57E-02	6.17E-02	1.16E-01	1.74E-01	1.94E-01	1.74E-01	1.21E-01				
	1.93E-13	5.59E-12	1.41E-10	3.00E-09	5.18E-08	7.08E-07	6.36E-06	4.15E-05	2.11E-03	8.33E-03	2.57E-02	6.22E-02	1.20E-01	1.86E-01	2.44E-01	2.79E-01	1.27E-01				
	4.00E-15	1.49E-13	8.48E-12	1.84E-10	2.92E-09	5.13E-08	7.07E-07	6.35E-06	4.15E-04	2.11E-03	8.36E-03	2.59E-02	6.40E-02	1.28E-01	2.18E-01	3.16E-01	2.23E-01				
3	$C_{10}H_{34}$	$C_{17}H_{36}$	$C_{18}H_{38}$	$C_{19}H_{40}$	$C_{20}H_{42}$	$C_{21}H_{44}$	$C_{22}H_{46}$	$C_{23}H_{48}$	$C_{24}H_{50}$	$C_{25}H_{52}$	$C_{26}H_{54}$	$C_{27}H_{56}$	$C_{28}H_{58}$	$C_{29}H_{60}$	$C_{30}H_{62}$	$C_{31}H_{64}$	$C_{32}H_{66}$				
	2.23E-01	1.73E-01	8.71E-02	5.56E-02	3.26E-02	1.74E-02	8.36E-03	3.62E-03	1.41E-03	4.96E-04	1.57E-04	4.54E-05	2.02E-05	2.95E-06	6.80E-07	1.48E-07					
	2.11E-01	1.82E-01	1.50E-01	8.20E-02	5.37E-02	3.20E-02	1.72E-02	8.34E-03	3.63E-03	1.42E-03	5.05E-04	1.63E-04	4.82E-05	1.32E-05	3.41E-06	8.31E-07					
	1.79E-01	1.73E-01	1.58E-01	8.13E-02	5.36E-02	3.20E-02	1.72E-02	8.33E-03	3.63E-03	1.42E-03	5.05E-04	1.63E-04	4.82E-05	1.32E-05	3.41E-06	8.31E-07					
	1.35E-01	1.46E-01	1.50E-01	8.12E-02	5.35E-02	3.20E-02	1.72E-02	8.33E-03	3.63E-03	1.42E-03	5.05E-04	1.63E-04	4.82E-05	1.32E-05	3.41E-06	8.31E-07					
	9.17E-02	1.11E-01	1.27E-01	1.36E-01	1.08E-01	7.92E-02	5.27E-02	3.17E-02	1.72E-02	8.36E-03	3.66E-03	1.45E-03	5.23E-04	1.73E-04	5.31E-05	1.53E-05	4.16E-06				
	5.56E-02	7.50E-02	9.59E-02	1.15E-01	1.28E-01	1.31E-01	1.21E-01	1.02E-01	7.70E-02	5.23											

	modal composition																
1	C ₆ H ₃₄	C ₇ H ₃₆	C ₈ H ₃₈	C ₉ H ₄₀	C ₂₀ H ₄₂	C ₂₁ H ₄₄	C ₂₂ H ₄₆	C ₂₃ H ₄₈	C ₂₄ H ₅₀	C ₂₅ H ₅₂	C ₂₆ H ₅₄	C ₂₇ H ₅₆	C ₂₈ H ₅₈	C ₂₉ H ₆₀	C ₃₀ H ₆₂	C ₃₁ H ₆₄	C ₃₂ H ₆₆
5.13E-01	2.31E-01	4.88E-02	3.99E-03	1.20E-04	1.34E-06	5.47E-09	8.22E-12	4.55E-15	9.25E-19	6.93E-23	1.91E-27	1.93E-32	7.20E-38	9.91E-44	5.29E-50	1.32E-56	
3.11E-01	3.81E-01	2.19E-01	4.86E-02	3.99E-03	1.20E-04	1.34E-06	5.47E-09	8.22E-12	4.55E-15	9.25E-19	6.93E-23	1.91E-27	1.93E-32	7.23E-38	1.05E-43	7.12E-50	
6.95E-02	2.31E-01	3.61E-01	2.18E-01	4.86E-02	3.99E-03	1.20E-04	1.34E-06	5.47E-09	8.22E-12	4.55E-15	9.25E-19	6.93E-23	1.91E-27	1.94E-32	7.65E-38	1.41E-43	
5.70E-03	5.16E-02	2.19E-01	3.59E-01	2.18E-01	4.86E-02	3.99E-03	1.20E-04	1.34E-06	5.47E-09	8.22E-12	4.55E-15	9.25E-19	6.93E-23	1.92E-27	2.05E-32	1.03E-37	
1.72E-04	4.24E-03	4.88E-02	2.18E-01	3.59E-01	2.18E-01	4.86E-02	3.99E-03	1.20E-04	1.34E-06	5.47E-09	8.22E-12	4.55E-15	9.25E-19	6.96E-23	2.03E-27	2.76E-32	
1.91E-06	1.28E-04	4.01E-02	4.86E-02	2.18E-01	3.59E-01	2.18E-01	4.86E-02	3.99E-03	1.20E-04	1.34E-06	5.47E-09	8.22E-12	4.55E-15	9.29E-19	7.36E-23	2.73E-27	
7.82E-09	1.42E-06	1.21E-04	3.99E-03	4.86E-02	2.18E-01	3.59E-01	2.18E-01	4.86E-02	3.99E-03	1.20E-04	1.34E-06	5.47E-09	8.22E-12	4.57E-15	9.83E-19	9.90E-23	
1.18E-11	5.81E-09	1.34E-08	1.20E-04	3.99E-03	4.86E-02	2.18E-01	3.59E-01	2.18E-01	4.86E-02	3.99E-03	1.20E-04	1.34E-06	5.47E-09	8.26E-12	4.83E-15	1.32E-18	
6.50E-15	8.73E-12	5.49E-09	1.34E-06	1.20E-03	3.99E-03	4.86E-02	2.18E-01	3.59E-01	2.18E-01	4.86E-02	3.99E-03	1.20E-04	1.34E-06	5.49E-09	8.73E-12	6.50E-15	
1.32E-15	4.83E-15	8.26E-12	5.47E-06	1.34E-06	1.20E-04	3.99E-03	4.86E-02	2.18E-01	3.59E-01	2.18E-01	4.86E-02	3.99E-03	1.20E-04	1.34E-06	5.81E-09	1.18E-11	
9.90E-23	9.83E-19	4.57E-15	5.47E-09	1.34E-06	1.20E-04	3.99E-03	4.86E-02	2.18E-01	3.59E-01	2.18E-01	4.86E-02	3.99E-03	1.21E-04	1.42E-06	7.82E-09		
2.73E-27	7.36E-23	9.29E-19	4.55E-15	8.22E-12	5.47E-09	1.34E-06	1.20E-04	3.99E-03	4.86E-02	2.18E-01	3.59E-01	2.18E-01	4.86E-02	4.01E-03	1.28E-04	1.91E-06	
2.76E-32	2.03E-27	6.96E-23	9.25E-19	4.55E-15	8.22E-12	5.47E-09	1.34E-06	1.20E-04	3.99E-03	4.86E-02	2.18E-01	3.59E-01	2.18E-01	4.88E-02	4.24E-03	1.72E-04	
1.03E-37	2.05E-32	1.92E-27	6.93E-23	9.25E-19	4.55E-15	8.22E-12	5.47E-09	1.34E-06	1.20E-04	3.99E-03	4.86E-02	2.18E-01	3.59E-01	2.19E-01	5.16E-02	5.70E-03	
1.41E-43	7.65E-32	1.94E-32	7.63E-27	9.35E-23	9.25E-19	4.55E-15	8.22E-12	5.47E-09	1.34E-06	1.20E-04	3.99E-03	4.86E-02	2.18E-01	3.61E-01	2.31E-01	6.95E-02	
7.12E-50	1.05E-43	7.23E-32	9.35E-32	1.91E-27	6.93E-23	9.25E-19	4.55E-15	8.22E-12	5.47E-09	1.34E-06	1.20E-04	3.99E-03	4.86E-02	2.19E-01	3.81E-01	3.11E-01	
1.32E-56	5.29E-50	9.91E-44	7.20E-38	1.93E-32	1.91E-27	6.93E-23	9.25E-19	4.55E-15	8.22E-12	5.47E-09	1.34E-06	1.20E-04	3.99E-03	4.88E-02	2.31E-01	5.13E-01	
2	C ₆ H ₃₄	C ₇ H ₃₆	C ₈ H ₃₈	C ₉ H ₄₀	C ₂₀ H ₄₂	C ₂₁ H ₄₄	C ₂₂ H ₄₆	C ₂₃ H ₄₈	C ₂₄ H ₅₀	C ₂₅ H ₅₂	C ₂₆ H ₅₄	C ₂₇ H ₅₆	C ₂₈ H ₅₈	C ₂₉ H ₆₀	C ₃₀ H ₆₂	C ₃₁ H ₆₄	C ₃₂ H ₆₆
2.99E-01	2.04E-01	1.21E-01	6.06E-02	4.24E-02	7.91E-03	2.00E-03	3.93E-04	6.02E-05	7.19E-06	6.69E-07	4.86E-08	2.77E-09	1.25E-10	4.58E-12	1.41E-13	3.79E-15	
2.64E-01	2.31E-01	1.77E-01	1.13E-01	5.90E-01	2.44E-02	7.89E-03	1.99E-03	6.02E-05	7.20E-06	6.71E-07	4.90E-08	2.84E-09	1.34E-10	5.30E-12	1.83E-13		
1.82E-01	2.04E-01	2.00E-01	1.65E-01	5.84E-02	2.43E-02	7.89E-03	1.99E-03	6.03E-05	7.21E-06	6.77E-07	5.04E-08	3.05E-09	1.55E-10	6.85E-12			
9.72E-02	1.40E-01	1.77E-01	1.87E-01	1.60E-01	1.09E-01	5.83E-02	2.43E-02	7.89E-03	1.99E-03	6.04E-05	7.28E-06	6.96E-07	5.40E-08	3.52E-09	2.00E-10		
4.05E-02	7.51E-02	1.21E-01	1.65E-01	1.82E-01	1.59E-01	1.09E-01	5.83E-02	2.43E-02	7.89E-03	2.00E-03	3.94E-04	6.05E-05	7.48E-06	7.46E-07	6.25E-08	4.56E-09	
1.32E-02	3.13E-02	6.50E-02	1.13E-01	1.60E-01	1.80E-01	1.59E-01	5.83E-02	2.43E-02	7.89E-03	2.00E-03	3.94E-04	6.26E-05	8.02E-06	8.62E-07	8.08E-08		
3.33E-03	1.02E-02	2.71E-02	6.06E-02	1.10E-01	1.59E-01	1.80E-01	1.58E-01	1.09E-01	5.83E-02	2.43E-02	7.91E-03	2.02E-03	4.08E-04	6.72E-05	9.27E-06	1.12E-06	
6.55E-04	2.57E-03	8.80E-03	2.53E-02	5.90E-02	1.09E-01	1.59E-01	1.80E-01	1.58E-01	1.09E-01	5.83E-02	2.44E-02	7.98E-03	2.07E-03	4.38E-04	7.76E-05	1.20E-05	
1.00E-04	5.06E-04	2.22E-03	8.20E-03	2.46E-02	5.84E-02	1.09E-01	1.58E-01	1.80E-01	1.58E-01	5.84E-02	2.46E-02	8.20E-03	2.22E-03	5.06E-04	1.00E-04		
1.20E-05	7.76E-05	4.38E-03	2.07E-03	7.98E-03	2.44E-02	5.83E-02	1.09E-01	1.58E-01	1.80E-01	1.59E-01	5.90E-02	2.53E-02	8.80E-03	2.57E-03	6.55E-04		
1.12E-06	9.27E-06	4.05E-04	2.02E-03	7.91E-03	2.43E-02	5.83E-02	1.09E-01	1.58E-01	1.80E-01	1.59E-01	5.90E-02	2.51E-02	8.71E-02	1.02E-02	3.33E-03		
8.08E-08	6.82E-07	8.02E-05	6.26E-05	3.97E-04	2.00E-03	7.89E-03	2.43E-02	5.83E-02	1.09E-01	1.59E-01	1.80E-01	1.60E-01	1.13E-01	6.50E-02	3.13E-02	1.32E-02	
4.56E-09	6.25E-08	7.46E-07	7.48E-07	6.09E-05	3.94E-04	2.00E-03	7.89E-03	2.43E-02	5.83E-02	1.09E-01	1.59E-01	1.80E-01	1.60E-01	1.13E-01	6.51E-02	4.05E-02	
2.00E-10	3.52E-09	5.40E-09	6.99E-07	7.28E-06	6.04E-05	3.93E-04	1.99E-03	7.89E-03	2.43E-02	5.83E-02	1.09E-01	1.59E-01	1.80E-01	1.60E-01	1.13E-01	6.72E-02	
6.85E-12	1.55E-10	3.05E-09	5.04E-08	6.77E-07	7.21E-06	6.03E-05	3.93E-04	1.99E-03	7.89E-03	2.43E-02	5.84E-02	1.09E-01	1.59E-01	1.80E-01	1.60E-01	1.13E-01	2.04E-01
1.83E-13	5.30E-12	1.34E-10	2.84E-09	4.90E-08	6.71E-07	7.20E-06	6.02E-05	3.93E-04	1.99E-03	7.89E-03	2.44E-02	5.90E-02	1.13E-01	1.77E-01	2.31E-01	2.64E-01	
3.79E-15	1.41E-13	4.58E-12	1.25E-10	2.77E-09	4.86E-08	6.69E-07	7.19E-06	6.02E-05	3.93E-04	1.99E-03	7.91E-03	2.46E-02	6.06E-02	1.21E-01	2.04E-01	2.99E-01	
3	C ₆ H ₃₄	C ₇ H ₃₆	C ₈ H ₃₈	C ₉ H ₄₀	C ₂₀ H ₄₂	C ₂₁ H ₄₄	C ₂₂ H ₄₆	C ₂₃ H ₄₈	C ₂₄ H ₅₀	C ₂₅ H ₅₂	C ₂₆ H ₅₄	C ₂₇ H ₅₆	C ₂₈ H ₅₈	C ₂₉ H ₆₀	C ₃₀ H ₆₂	C ₃₁ H ₆₄	C ₃₂ H ₆₆
2.11E-01	1.64E-01	1.20E-01	8.25E-02	5.27E-02	3.09E-02	1.64E-02	7.92E-03	3.43E-03	4.70E-04	4.49E-07	4.30E-05	1.14E-05	2.80E-06	6.44E-07	1.41E-07		
2.00E-01	1.73E-01	1.42E-01	1.09E-01	7.77E-02	5.09E-02	3.03E-02	1.63E-02	7.90E-03	3.44E-03	4.78E-04	4.54E-05	1.25E-05	3.23E-06	7.87E-07			
1.69E-01	1.64E-01	1.50E-01	1.29E-01	1.03E-01	7.51E-02	5.00E-02	3.00E-02	1.63E-02	7.92E-03	3.47E-03	4.95E-04	4.64E-05	5.03E-05	1.45E-05	3.94E-06		
1.28E-01	1.38E-01	1.42E-01	1.36E-01	1.21E-01	9.91E-02	7.37E-02	4.95E-02	3.00E-02	1.63E-02	7.99E-03	3.53E-03	5.12E-04	5.26E-04	5.80E-05	1.77E-05		
5.27E-02	7.11E-02	9.09E-02	1.09E-01	1.21E-01	1.17E-01	9.73E-02	7.31E-02	4.95E-02	3.02E-02	1.67E-02	8.02E-03	3.59E-03	4.89E-03	4.28E-03	1.92E-03	8.17E-04	
1.39E-02	2.34E-02	3.74E-02	5.59E-02	7.77E-02	9.91E-02	1.15E-01	1.20E-01	1.41E-01	9.65E-02	7.37E-02	5.09E-02	3.19E-02	1.84E-02	9.85E-03	2.35E-03		
6.04E-03	1.14E-02	2.03E-02	5.32E-02	5.27E-02	7.51E-02	9.73E-02	1.14E-01	1.20E-01	1.41E-01	9.73E-02	7.51E-02	5.27E-02	3.39E-02	2.03E-02	1.14E-02	6.04E-03	
2.35E-03	9.49E-03	9.85E-03	1.84E-02	3.19E-02	5.09E-02	7.37E-02	9.65E-02	1.14E-01	1.20E-01	1.41E-01	9.91E-02</td						

		modal composition																		
		C ₁₆ H ₃₄	C ₁₇ H ₃₅	C ₁₈ H ₃₈	C ₁₉ H ₄₀	C ₂₀ H ₄₂	C ₂₁ H ₄₄	C ₂₂ H ₄₆	C ₂₃ H ₄₈	C ₂₄ H ₅₀	C ₂₅ H ₅₂	C ₂₆ H ₅₄	C ₂₇ H ₅₆	C ₂₈ H ₅₈	C ₂₉ H ₆₀	C ₃₀ H ₆₂	C ₃₁ H ₆₄	C ₃₂ H ₆₆		
1		5.70E-02	2.57E-02	5.42E-03	4.43E-04	1.34E-05	1.49E-07	6.08E-10	9.13E-13	5.05E-16	1.03E-19	7.69E-24	2.12E-28	2.15E-33	8.00E-39	1.10E-44	5.87E-51	1.47E-57		
		3.46E-02	4.24E-02	2.43E-02	5.40E-03	4.43E-04	1.34E-05	1.49E-07	6.08E-10	9.13E-13	5.05E-16	1.03E-19	7.69E-24	2.12E-28	2.15E-33	8.50E-39	1.57E-44			
		7.72E-03	2.57E-02	4.01E-02	2.42E-02	5.40E-03	4.43E-04	1.34E-05	1.49E-07	6.08E-10	9.13E-13	5.05E-16	1.03E-19	7.69E-24	2.12E-28	2.16E-33	8.50E-39	1.57E-44		
		6.34E-04	5.73E-03	2.43E-02	3.99E-02	2.42E-02	5.40E-03	4.43E-04	1.34E-05	1.49E-07	6.08E-10	9.13E-13	5.05E-16	1.03E-19	7.70E-24	2.13E-28	2.28E-33	1.14E-38		
		1.91E-05	4.71E-04	5.42E-03	2.42E-02	3.99E-02	2.42E-02	5.40E-03	4.43E-04	1.34E-05	1.49E-07	6.08E-10	9.13E-13	5.05E-16	1.03E-19	7.73E-24	2.25E-28	3.07E-33		
		2.13E-07	1.42E-05	4.45E-04	5.40E-03	2.42E-02	3.99E-02	2.42E-02	5.40E-03	4.43E-04	1.34E-05	1.49E-07	6.08E-10	9.13E-13	5.05E-16	1.03E-19	8.17E-24	3.03E-28		
		8.69E-10	1.58E-07	1.34E-05	4.43E-04	5.40E-03	2.42E-02	3.99E-02	2.42E-02	5.40E-03	4.43E-04	1.34E-05	1.49E-07	6.08E-10	9.14E-13	5.08E-16	1.09E-19	1.10E-23		
		1.31E-12	6.45E-10	1.49E-07	1.34E-05	4.42E-04	5.40E-03	2.42E-02	3.99E-02	2.42E-02	5.40E-03	4.42E-04	1.34E-05	1.49E-07	6.08E-10	9.18E-13	5.37E-16	1.47E-19		
		7.22E-16	9.70E-13	6.10E-10	1.49E-07	1.34E-05	4.43E-04	5.40E-03	2.42E-02	3.99E-02	2.42E-02	5.40E-03	4.43E-04	1.34E-05	1.49E-07	6.10E-10	9.70E-13	7.22E-16		
		1.47E-19	5.37E-16	9.18E-13	6.08E-10	1.49E-07	1.34E-05	4.43E-04	5.40E-03	2.42E-02	3.99E-02	2.42E-02	5.40E-03	4.43E-04	1.34E-05	1.49E-07	6.45E-10	1.31E-12		
		1.10E-23	1.09E-19	5.08E-16	9.14E-13	6.08E-10	1.49E-07	1.34E-05	4.43E-04	5.40E-03	2.42E-02	3.99E-02	2.42E-02	5.40E-03	4.43E-04	1.34E-05	1.58E-07	8.69E-10		
		3.03E-28	8.17E-24	1.03E-19	5.05E-16	9.13E-13	6.08E-10	1.49E-07	1.34E-05	4.43E-04	5.40E-03	2.42E-02	3.99E-02	2.42E-02	5.40E-03	4.43E-04	1.42E-05	2.13E-07		
		3.07E-33	2.25E-28	7.73E-24	1.03E-19	5.05E-16	9.13E-13	6.08E-10	1.49E-07	1.34E-05	4.43E-04	5.40E-03	2.42E-02	3.99E-02	2.42E-02	5.42E-03	4.71E-04	1.91E-05		
		1.14E-38	2.28E-33	2.13E-28	7.70E-24	1.03E-19	5.05E-16	9.13E-13	6.08E-10	1.49E-07	1.34E-05	4.43E-04	5.40E-03	2.42E-02	3.99E-02	2.43E-02	5.73E-03	6.34E-04		
		1.57E-44	8.50E-39	2.16E-33	2.12E-28	7.69E-24	1.03E-19	5.05E-16	9.13E-13	6.08E-10	1.49E-07	1.34E-05	4.43E-04	5.40E-03	2.42E-02	4.01E-02	2.57E-02	7.72E-03		
		7.91E-51	1.16E-44	8.04E-39	2.15E-33	2.12E-28	7.69E-24	1.03E-19	5.05E-16	9.13E-13	6.08E-10	1.49E-07	1.34E-05	4.43E-04	5.40E-03	2.43E-02	4.24E-02	3.46E-02		
		1.47E-57	5.87E-51	1.10E-44	8.00E-39	2.15E-33	2.12E-28	7.69E-24	1.03E-19	5.05E-16	9.13E-13	6.08E-10	1.49E-07	1.34E-05	4.43E-04	5.42E-03	2.57E-02	5.70E-02		
2		C ₁₆ H ₃₄	C ₁₇ H ₃₅	C ₁₈ H ₃₈	C ₁₉ H ₄₀	C ₂₀ H ₄₂	C ₂₁ H ₄₄	C ₂₂ H ₄₆	C ₂₃ H ₄₈	C ₂₄ H ₅₀	C ₂₅ H ₅₂	C ₂₆ H ₅₄	C ₂₇ H ₅₆	C ₂₈ H ₅₈	C ₂₉ H ₆₀	C ₃₀ H ₆₂	C ₃₁ H ₆₄	C ₃₂ H ₆₆		
		3.33E-02	2.27E-02	1.35E-02	6.74E-03	2.73E-03	8.79E-04	2.22E-04	4.36E-05	6.69E-06	7.99E-07	7.44E-08	5.40E-09	3.07E-09	1.39E-11	5.09E-13	1.57E-14	4.21E-16		
		2.94E-02	2.57E-02	1.96E-02	6.55E-03	2.71E-03	8.77E-04	2.22E-04	4.36E-05	6.69E-06	8.00E-07	7.45E-08	5.45E-09	3.16E-10	1.49E-11	5.89E-13	2.03E-14			
		2.02E-02	2.27E-02	2.22E-02	1.83E-02	1.22E-02	6.49E-03	2.70E-03	8.76E-04	2.22E-04	4.36E-05	6.69E-06	8.01E-07	7.52E-08	5.60E-09	3.39E-10	1.72E-11	7.62E-13		
		1.08E-02	1.56E-02	1.96E-02	2.07E-02	1.78E-02	1.21E-02	6.48E-03	2.70E-03	8.76E-04	2.22E-04	4.37E-05	6.71E-06	8.08E-07	7.73E-08	6.00E-09	3.92E-10	2.23E-11		
		4.50E-03	8.35E-03	1.35E-02	2.02E-02	1.77E-02	1.21E-02	6.48E-03	2.70E-03	8.76E-04	2.22E-04	4.38E-05	6.77E-06	8.13E-07	8.29E-08	6.94E-09	5.07E-10			
		1.46E-03	3.48E-03	7.22E-03	1.26E-02	1.78E-02	2.00E-02	1.76E-02	1.21E-02	6.48E-03	2.70E-03	8.77E-04	2.22E-04	4.41E-05	6.96E-06	8.91E-07	9.58E-08	8.98E-09		
		3.69E-04	1.13E-03	3.01E-03	6.74E-03	1.22E-02	1.77E-02	2.00E-02	1.76E-02	1.21E-02	6.48E-03	2.70E-03	8.79E-04	2.24E-04	4.54E-05	7.46E-06	1.03E-06	1.24E-07		
		7.28E-05	2.86E-04	9.77E-04	2.81E-03	6.55E-03	1.21E-02	1.76E-02	1.99E-02	1.76E-02	1.21E-02	6.48E-03	2.71E-03	8.87E-04	2.30E-04	4.87E-05	8.63E-06	1.33E-06		
		1.12E-05	5.62E-05	2.47E-04	9.11E-04	2.73E-03	6.49E-03	1.21E-02	1.76E-02	1.99E-02	1.76E-02	1.21E-02	6.49E-03	2.71E-03	9.11E-04	2.47E-04	5.62E-05	1.12E-05		
		1.33E-06	6.83E-06	4.87E-05	2.30E-04	8.87E-04	2.71E-03	6.48E-03	1.21E-02	1.76E-02	1.99E-02	1.76E-02	1.21E-02	6.48E-03	2.71E-03	9.17E-04	2.86E-04	7.28E-05		
		1.24E-07	1.03E-06	7.46E-06	4.54E-05	2.24E-04	8.79E-04	2.70E-03	6.48E-03	1.21E-02	1.76E-02	1.99E-02	1.76E-02	1.21E-02	6.48E-03	2.71E-03	9.13E-04	3.13E-03	3.69E-04	
		8.98E-09	5.98E-08	8.91E-07	6.96E-06	4.41E-05	2.22E-04	8.77E-04	2.70E-03	6.48E-03	1.21E-02	1.76E-02	1.99E-02	1.76E-02	1.21E-02	6.48E-03	2.71E-03	9.12E-04	3.46E-03	
		5.07E-10	6.94E-09	8.29E-08	8.31E-07	6.77E-06	4.38E-05	2.22E-04	8.76E-04	2.70E-03	6.48E-03	1.21E-02	1.76E-02	1.99E-02	1.76E-02	1.21E-02	6.48E-03	2.71E-03	9.11E-04	
		2.23E-11	3.92E-10	6.00E-09	7.73E-08	8.08E-07	6.71E-06	4.37E-05	2.22E-04	8.76E-04	2.70E-03	6.48E-03	1.21E-02	1.76E-02	1.99E-02	1.76E-02	1.21E-02	6.48E-03	2.71E-03	
		7.62E-13	1.72E-11	3.39E-10	5.60E-09	7.52E-08	8.01E-07	6.69E-06	4.36E-05	2.22E-04	8.76E-04	2.70E-03	6.49E-03	1.22E-02	1.76E-02	1.99E-02	1.76E-02	1.22E-02	6.48E-03	
		2.03E-14	5.89E-13	1.49E-11	3.16E-10	5.16E-09	5.45E-08	7.45E-07	8.05E-06	4.35E-05	2.22E-04	8.76E-04	2.70E-03	6.50E-03	1.23E-02	1.76E-02	1.99E-02	1.76E-02	1.23E-02	6.48E-03
		1.56E-08	7.16E-08	3.11E-07	1.26E-06	4.78E-06	1.66E-05	5.22E-05	8.03E-04	4.34E-05	2.22E-04	8.76E-04	2.70E-03	6.51E-03	1.24E-02	1.76E-02	1.99E-02	1.76E-02	1.24E-02	6.48E-03
3		C ₁₆ H ₃₄	C ₁₇ H ₃₅	C ₁₈ H ₃₈	C ₁₉ H ₄₀	C ₂₀ H ₄₂	C ₂₁ H ₄₄	C ₂₂ H ₄₆	C ₂₃ H ₄₈	C ₂₄ H ₅₀	C ₂₅ H ₅₂	C ₂₆ H ₅₄	C ₂₇ H ₅₆	C ₂₈ H ₅₈	C ₂₉ H ₆₀	C ₃₀ H ₆₂	C ₃₁ H ₆₄	C ₃₂ H ₆₆		
		2.35E-02	1.82E-02	9.17E-03	5.85E-03	3.43E-03	1.83E-03	8.80E-04	3.82E-04	1.49E-04	5.22E-05	1.66E-05	4.78E-06	1.26E-06	3.11E-07	7.16E-08	1.56E-08			
		2.22E-02	1.92E-02	1.57E-02	1.21E-02	8.63E-03	5.65E-03	3.37E-03	1.81E-03	8.78E-04	3.82E-04	1.50E-04	5.32E-05	1.71E-05	5.07E-06	1.39E-06	3.59E-07	8.75E-08		
		1.88E-02	1.82E-02	1.66E-02	1.43E-02	1.14E-02	8.34E-03	5.55E-03	3.34E-03	1.81E-03	8.80E-04	3.86E-04	1.53E-04	5.50E-05	1.82E-05	5.58E-06	1.61E-06	4.38E-07		
		1.42E-02	1.54E-02	1.57E-02	1.51E-02	1.35E-02	8.19E-03	5.50E-03	3.33E-03	1.81E-03	8.87E-04	3.93E-04	1.58E-04	5.85E-05	2.00E-05	6.44E-06	1.96E-06			
		9.65E-03	1.17E-02	1.33E-02	1.43E-02	1.42E-02	1.30E-02	8.12E-03	5.49E-03	3.34E-03	1.83E-03	9.04E-04	4.07E-04	1.68E-04	6.44E-05	2.31E-05	7.87			

n-alkanes C _n H _(2n+2)	Chickos&Lipkind 2008	EPI Suite	A) Nannooolal et al 2008			B) Myrdal and Yalkowsky 1997			Co) Compernolle et al 2011 for all boiling points	
			boiling point			boiling point				
			a	b	c	a	b	c		
16		9.29E-001	2.87E-001	6.63E-001	5.38E-001	1.39E-001	3.46E-001	2.75E-001	3.05E-001	
17		4.32E-001	6.85E-002	2.45E-001	2.06E-001	3.14E-002	1.24E-001	1.03E-001	9.98E-002	
18		1.95E-001	1.54E-002	9.22E-002	7.91E-002	6.74E-003	4.55E-002	3.86E-002	3.27E-002	
19		8.97E-002	3.23E-003	3.54E-002	3.04E-002	1.38E-003	1.73E-002	1.47E-002	1.07E-002	
20		4.13E-002	6.33E-004	1.39E-002	1.17E-002	2.70E-004	6.76E-003	5.61E-003	3.50E-003	
21	6.93E-004	1.89E-002	1.16E-004	5.60E-003	4.47E-003	5.03E-005	2.73E-003	2.16E-003	1.15E-003	
22	2.09E-004	9.23E-003	1.97E-005	2.26E-003	1.71E-003	8.94E-006	1.11E-003	8.35E-004	3.75E-004	
23	6.95E-005	4.73E-003	3.10E-006	8.86E-004	6.52E-004	1.52E-006	4.45E-004	3.25E-004	1.23E-004	
24	2.31E-005	2.26E-003	4.50E-007	3.39E-004	2.48E-004	2.46E-007	1.75E-004	1.27E-004	4.01E-005	
25	8.51E-006	1.28E-002	6.01E-008	1.26E-004	9.38E-005	3.81E-008	6.71E-005	4.97E-005	1.31E-005	
26	2.83E-006	7.02E-004	7.37E-009	4.58E-005	3.53E-005	5.64E-009	2.53E-005	1.95E-005	4.30E-006	
27	1.15E-006	1.31E-004	8.25E-010	1.61E-005	1.32E-005	7.97E-010	9.36E-006	7.68E-006	1.41E-006	
28	3.14E-007	2.06E-004	8.40E-011	5.53E-006	4.94E-006	1.08E-010	3.39E-006	3.03E-006	4.61E-007	
29	1.05E-007	1.27E-004	7.74E-012	1.84E-006	1.83E-006	1.39E-011	1.20E-006	1.20E-006	1.51E-007	
30	3.48E-008	7.49E-005	6.44E-013	5.96E-007	6.75E-007	1.72E-012	4.20E-007	4.74E-007	4.93E-008	
31	1.16E-008	4.54E-005	4.81E-014	1.87E-007	2.47E-007	2.03E-013	1.43E-007	1.88E-007	1.61E-008	
32	3.49E-009	2.66E-005	3.20E-015	5.70E-008	9.01E-008	2.29E-014	4.80E-008	7.43E-008	5.28E-009	

Table 5-S. Vapour pressure data at 298 K from different sources corresponding to Figure 2 in the main manuscript. a, b, and c refer to the boiling point of Joback and Reid (1987), Stein and Brown (1994) and Nannooolal et al. (2004), respectively. A-a, B-c and Co are used in this study.

compound	vapour
C ₁₆ H ₃₄	6.42 (3.62)
C ₁₇ H ₃₆	9.32 (4.31)
C ₁₈ H ₃₈	9.36 (4.41)
C ₁₉ H ₄₀	9.74 (4.09)
C ₂₀ H ₄₂	8.35 (3.59)
C ₂₁ H ₄₄	6.20 (3.06)
C ₂₂ H ₄₆	3.97 (1.98)
C ₂₃ H ₄₈	2.32 (1.25)
C ₂₄ H ₅₀	1.59 (1.79)
C ₂₅ H ₅₂	1.20 (0.52)
C ₂₆ H ₅₄	1.00 (0.50)
C ₂₇ H ₅₆	1.28 (0.53)
C ₂₈ H ₅₈	1.03 (0.53)
C ₂₉ H ₆₀	1.24 (0.53)
C ₃₀ H ₆₂	0.80 (0.38)
C ₃₁ H ₆₄	0.77 (0.30)
C ₃₂ H ₆₆	0.42 (0.18)

1291 *Table 6-S. Gas-phase concentrations used in the model. Numbers in parenthesis show the standard deviation of the*
 1292 *measurements. Unit, ng m⁻³.*